

DRAGON: Determining Regulatory Associations using Graphical models on multi-Omic Networks

Deborah Weighill^{1,*†}, Rebekka Burkholz^{1,*}, Marouen Ben Guebila¹, Helena U. Zacharias^{2,3}, John Quackenbush^{1,***}, and Michael Altenbuchinger^{1,4,***}

¹Department of Biostatistics, Harvard T.H. Chan School of Public Health, Boston, MA, USA

²Department of Internal Medicine I, University Medical Center Schleswig-Holstein, Campus Kiel, Kiel, Germany

³Institute of Clinical Molecular Biology, Kiel University and University Medical Center Schleswig-Holstein, Campus Kiel, Kiel, Germany

⁴Research Group Computational Biology, University of Hohenheim, Stuttgart, Germany

[†]Current address: Lineberger Comprehensive Cancer Center, University of North Carolina at Chapel Hill, Chapel Hill, NC, USA

^{*}authors contributed equally to this work

^{**}shared senior authors

Abstract

The increasing quantity of multi-omics data, such as methylomic and transcriptomic profiles, collected on the same specimen, or even on the same cell, provide a unique opportunity to explore the complex interactions that define cell phenotype and govern cellular responses to perturbations. We propose a network approach based on Gaussian Graphical Models (GGMs) that facilitates the joint analysis of paired omics data. This method, called **DRAGON** (Determining Regulatory Associations using Graphical models on multi-Omic Networks), calibrates its parameters to achieve an optimal trade-off between the network's complexity and estimation accuracy, while explicitly accounting for the characteristics of each of the assessed omics layers. In simulation studies, we show that DRAGON adapts to edge-density and feature-size differences between the omics layers, which improves model inference and the recovery of associations compared to state-of-the-art network inference using GGMs. Next, we verified this performance gain on paired single-cell data, where the transcriptome was assayed together with selected proteins. Finally, we used DRAGON to study joint transcriptome–methylome data of breast cancer specimens. In this context, we provide examples of how DRAGON can identify key molecular mechanisms. For instance, we show how co-expression can be explained by co-methylation and how DRAGON gives hints about the spatial organization of the genome. DRAGON is available as open-source code in python through the Network Zoo package (netZooPy v0.8; [netzoo.github.io](https://github.com/netzoo/netzoo))

1 Introduction

Many features of biological systems can be visualized as networks, where biologically relevant elements are represented as nodes and relationships between those elements as edges. Examples include gene-regulatory networks, which represent the regulation of genes by transcription factors, and protein–protein interaction networks, which capture physical interactions between proteins [1, 2]. Network models can either be based on prior knowledge [3] or inferred from data [4], or combinations thereof [5].

Here, we focus on data-based network inference. More precisely, we concentrate on network inference using high-throughput omics data from bulk tissue or single cells. In this context, co-expression networks [6], which are based on a measure of correlation such as Pearson's correlation, are often used to capture potential associations between genes. A major drawback of co-expression networks is that they do not

distinguish direct from indirect effects [7]. To illustrate why this occurs, consider a situation where expression of gene A strongly correlates with that of both genes B and C , then naturally B correlates with C , even if there is no meaningful relationship between them. For example, A could be a transcription factor that regulates the expression of both B and C . In this case, erroneously, correlation indicates a relation between B and C although that implied relationship is only a consequence of their independent relationship to A . The problem of such erroneous correlations was discussed by Pearson and Yule in the early 20th century, where the term “spurious correlation” was introduced to distinguish indirect from direct, genuine relationships. For a historical review see [8].

Several approaches have attempted to address this issue [9, 10, 11, 12], of which partial correlation networks [11, 12] are among the most widely used methods. They have been demonstrated to outperform simple correlation networks [13], and were consistently among the best in comparison to other methods [14]. Intuitively, the partial correlation between two variables can be considered as the correlation that takes into account the effect of all remaining variables in the data set. Thus, it can distinguish a direct relationship from one that is mediated by one or more other variables.

Two major issues complicate the inference of partial correlation networks. The first is that omics data generally provide only part of the information necessary to distinguish between direct and incidental relationships. We know that gene regulation is a process that involves multiple “tiers” or layers of control, including transcription factor binding, epigenetic regulation, and chromatin structure. However, we generally have only gene expression data and not the other regulatory data that could help to prevent the possibly erroneous conclusion that groups of genes are co-related when their expression is simply correlated, which could occur by chance or through the action of combinations of other factors. Thus, correct inference of direct and indirect relationships often require additional data, which is generally not possible to generate on a single sample.

However, new technologies are making it possible to generate additional layers of omics data on the same samples. For example, The Cancer Genome Atlas (TCGA) provides data on RNA expression, methylation levels, and copy number variations for many individual tumor samples. More recently, it has become possible to assay different omics data types from individual cells, as demonstrated in [15], where the RNA and chromatin accessibility was measured in single cells. Such multifactorial data will allow us to better disentangle interactions between biological variables and distinguish genuine from spurious associations.

The second issue is the high dimensionality of omics data. The number of measured variables p often substantially exceeds the number of samples n (or both are of the same order of magnitude), presenting substantial challenges for the network inference [7]. Several remedies have been proposed based on regularization techniques from high-dimensional statistics [11, 12, 16, 17], but these often fail when adding omics layers; these failures are driven by a number of factors including the even larger numbers of variables, different numbers of variables for each omics layer, variable noise levels, and different edge densities in each data type.

Here, we propose a machine learning method to estimate partial correlation networks using several omics layers simultaneously. This method, **DRAGON** (Determining Regulatory Associations using Graphical models on multi-Omic Networks), calibrates its parameters to achieve an optimal trade-off between model complexity and estimation accuracy, while explicitly taking into account the unique characteristics of each omics layer.

We use simulation studies to show that DRAGON adapts to differences in edge densities and feature sizes of the included omics layers. We then apply DRAGON to paired transcriptome–protein single-cell data where we show that DRAGON outperforms network inference methods that use Gaussian Graphical Models (GGMs). Finally, we use DRAGON to analyze joint transcriptome–methylome data from TCGA breast cancer specimens. There, we show that DRAGON can identify potential regulatory molecular mechanisms, such as the association between gene co-methylation and co-expression. We also use DRAGON to identify features reflecting the short- and long-range spatial organization of the genome.

2 Materials and Methods

2.1 The Gaussian Graphical Model

Let X be a $n \times p$ data matrix of n observations and p features. Assume that the observations $\mathbf{x}_1, \mathbf{x}_2, \dots, \mathbf{x}_n \in \mathbb{R}^p$ are independent and identically distributed according to a multivariate normal, $N(\mu, \Sigma)$, where Σ is a positive definite covariance matrix. Further, $\Theta = (\theta_{ij}) = \Sigma^{-1}$ is the inverse covariance matrix (also called precision matrix) where vanishing entries θ_{ij} correspond to conditional independencies between variables i and j . A Gaussian Graphical Model (GGM) estimates conditional dependencies (or conversely, independencies) as a graph, where nodes represent variables and edges connect conditionally dependent pairs of variables [18, 19].

Let $S = \frac{1}{n} \sum_{i=1}^n (\mathbf{x}_i - \hat{\mu})(\mathbf{x}_i - \hat{\mu})^T$ be the sample covariance matrix, where $\hat{\mu} = \frac{1}{n} \sum_{i=1}^n \mathbf{x}_i$ is the sample mean. Then, the corresponding log likelihood takes the form

$$l(\Theta) = \frac{n}{2} (\log |\Theta| - \text{Tr}(S\Theta)). \quad (1)$$

The Maximum Likelihood Estimate (MLE) of Eq. (1) yields $\Theta = S^{-1}$.

2.2 Covariance shrinkage

If the number of variables p exceeds the number of independent measurements n , then S is singular and cannot be inverted. Even if p is smaller than n but of the same order of magnitude, the MLE of Θ has a high variance. The latter can be reduced by introducing a bias on Θ by adding regularization terms to Eq. (1), as for example proposed in [17]. Here, we follow the approach of [12] and shrink the covariance matrix. This yields the biased estimate

$$\hat{\Theta} = ((1 - \lambda)S + \lambda T)^{-1}, \quad (2)$$

where $\lambda \in [0, 1]$ is the regularization parameter and T is the target matrix. Here, different choices for T were proposed, such as the identity, $T = I_p$, and the diagonal of S , i.e. $T = \text{diag}(s_{11}, s_{22}, \dots, s_{pp})$. Throughout this article, we use the latter choice following the arguments in [12]. The penalty parameter λ can be estimated using the Lemma of Ledoit & Wolf [20].

2.3 DRAGON

2.3.1 Generalized covariance shrinkage

In DRAGON, we extend covariance shrinkage to account for two omics layers. For this purpose, we introduce layer specific regularization terms. Let $X^{(1)}$ be a $n \times p_1$ data matrix that represents the first omics layer and let $X^{(2)}$ be a $n \times p_2$ data matrix for the second layer, where p_1 and p_2 are the number of variables from omics technology 1 and 2. We further assume paired data meaning that measurements (rows) $\mathbf{x}_i^{(1)}$ and $\mathbf{x}_i^{(2)}$ correspond to the same sample i but differ in their features. We further define the empirical covariances $S^{(k,l)} = \frac{1}{n} \sum_{i=1}^n (\mathbf{x}_i^{(k)} - \hat{\mu}^{(k)})(\mathbf{x}_i^{(l)} - \hat{\mu}^{(l)})^T$ with the empirical mean vector $\hat{\mu}^{(k)} = \frac{1}{n} \sum_{i=1}^n \mathbf{x}_i^{(k)}$ for $k, l \in \{1, 2\}$. Now, we can generalize the shrinkage estimator to

$$\begin{aligned} \hat{\Theta} = & \left(\begin{pmatrix} (1 - \lambda_1)S^{(1,1)} & \sqrt{1 - \lambda_1}\sqrt{1 - \lambda_2}S^{(1,2)} \\ \sqrt{1 - \lambda_1}\sqrt{1 - \lambda_2}S^{(2,1)} & (1 - \lambda_2)S^{(2,2)} \end{pmatrix} \right. \\ & \left. + \begin{pmatrix} \lambda_1 T^{(1)} & 0 \\ 0 & \lambda_2 T^{(2)} \end{pmatrix} \right)^{-1}, \end{aligned} \quad (3)$$

with $\lambda_k \in [0, 1]$ and $T^{(k)} = \text{diag}(s_{11}^{(k)}, s_{22}^{(k)}, \dots, s_{p_k p_k}^{(k)})$, where $S^{(k,k)} = (s_{ij}^{(k)})$. For illustration purposes, we first consider the limit $\lambda_2 = 1$. Here, Eq. (3) becomes

$$\begin{aligned} \hat{\Theta} = & \left(\begin{pmatrix} (1 - \lambda_1)S^{(1,1)} & 0 \\ 0 & 0 \end{pmatrix} + \begin{pmatrix} \lambda_1 T^{(1)} & 0 \\ 0 & T^{(2)} \end{pmatrix} \right)^{-1} \\ = & \begin{pmatrix} \Theta^{(1,1)} & 0 \\ 0 & (T^{(2)})^{-1} \end{pmatrix}, \end{aligned} \quad (4)$$

where $\Theta^{(1,1)} = ((1 - \lambda_1)S^{(1,1)} + \lambda_1 T^{(1)})^{-1}$ is the shrinkage estimator of the precision matrix using only the features with $k = 1$. Thus, if $\lambda_2 = 1$, technology 1 decouples from technology 2.

Next, consider the limit $\lambda_1 = \lambda_2 = \lambda$. Then Eq. (3) becomes

$$\begin{aligned}\hat{\Theta} &= \left((1 - \lambda) \begin{pmatrix} S^{(1,1)} & S^{(1,2)} \\ S^{(2,1)} & S^{(2,2)} \end{pmatrix} + \lambda \begin{pmatrix} T^{(1)} & 0 \\ 0 & T^{(2)} \end{pmatrix} \right)^{-1} \\ &= ((1 - \lambda)S + \lambda T)^{-1}.\end{aligned}\quad (5)$$

Thus, we naively treat both omics layers as if they were generated using the same technology. As such, DRAGON naturally incorporates two limits (i) GGMs estimated for the two omics layers separately and (ii) a GGM treating both layers such as if they belong to the same layer.

2.3.2 Generalization of the Lemma of Ledoit & Wolf

The penalty parameters λ_1 and λ_2 can be estimated using cross-validation, which is, however, computationally expensive. Alternatively, one can use an analytical estimate following the arguments of Ledoit & Wolf [20]. There, the shrinkage parameter λ was derived by minimizing

$$R = E \left[\|\hat{\Sigma} - \Sigma\|_F^2 \right] \quad (6)$$

with respect to λ , where $\hat{\Sigma} = (1 - \lambda)S + \lambda T$ and Σ is the true, underlying covariance. This is possible since $\text{bias}(S) = 0$ makes Eq. (6) independent of Σ .

Here, we extend this approach to the shrinkage formula (3) and estimate λ_1 and λ_2 by minimizing

$$E \left[\|\hat{\Sigma} - \Sigma\|_F^2 \right] = \sum_{k,l=1}^2 E \left[\|\hat{\Sigma}^{(k,l)} - \Sigma^{(k,l)}\|_F^2 \right] \quad (7)$$

with respect to λ_1 and λ_2 , where $\|\cdot\|_F$ is the Frobenius norm. Following the arguments in [12], we obtain

$$\begin{aligned}R &= E \left[\|\hat{\Sigma} - \Sigma\|_F^2 \right] \\ &= \text{const.} + \lambda_1 T_1^{(1)} + \lambda_2 T_1^{(2)} + \lambda_1^2 T_2^{(1)} + \lambda_2^2 T_2^{(2)} \\ &\quad + \lambda_1 \lambda_2 T_3 + \sqrt{1 - \lambda_1} \sqrt{1 - \lambda_2} T_4\end{aligned}\quad (8)$$

where the constant term is independent of λ_1 and λ_2 , and

$$\begin{aligned}T_1^{(k)} &= -2 \left(\sum_{i \neq j} \text{var}(s_{ij}^{(k)}) + \sum_{i,j} E((s_{ij}^{(1,2)})^2) \right), \\ T_2^{(k)} &= \sum_{i \neq j} E((s_{ij}^{(k)})^2), \\ T_3 &= 2 \sum_{i,j} E((s_{ij}^{(1,2)})^2), \\ T_4 &= 4 \sum_{i,j} \left(\text{var}(s_{ij}^{(1,2)}) - E((s_{ij}^{(1,2)})^2) \right)\end{aligned}$$

Eq. (8) can be easily minimized with respect to $\lambda_1 \in [0, 1]$ and $\lambda_2 \in [0, 1]$, where the moments can be estimated following [12].

2.3.3 Hypotheses testing

An estimate for the partial correlation between variable i and j can be directly obtained from $\hat{\Theta} = (\hat{\theta}_{ij})$ by calculating

$$\hat{\rho}_{ij} = -\frac{\hat{\theta}_{ij}}{\sqrt{\hat{\theta}_{ii}\hat{\theta}_{jj}}}. \quad (9)$$

As a consequence of covariance shrinkage, also the partial correlation matrix $\hat{P} = (\hat{\rho}_{ij})$ is shrunken [21]. A null-model probability density that naturally accounts for this shrinkage effect is

$$f_0^\lambda(\rho) = \frac{((1-\lambda)^2 - \rho^2)^{(\kappa-3)/2}}{\text{Beta}(\frac{1}{2}, \frac{\kappa-1}{2})(1-\lambda)^{\kappa-2}}, \quad (10)$$

where the parameter κ is given by $n - 1 - (p - 2)$ for $n \gg p$, or can be fitted by MLE for the ill-posed case $p < n$ or for $p \approx n$ [21]. Let

$$\hat{\Theta} = \begin{pmatrix} \hat{\Theta}^{(1,1)} & \hat{\Theta}^{(1,2)} \\ \hat{\Theta}^{(2,1)} & \hat{\Theta}^{(2,2)} \end{pmatrix} \quad \text{and} \quad \hat{P} = \begin{pmatrix} \hat{P}^{(1,1)} & \hat{P}^{(1,2)} \\ \hat{P}^{(2,1)} & \hat{P}^{(2,2)} \end{pmatrix}, \quad (11)$$

where $\hat{\Theta}^{(1,1)}$ ($\hat{P}^{(1,1)}$) has dimension $p_1 \times p_1$ and $\hat{\Theta}^{(2,2)}$ ($\hat{P}^{(2,2)}$) dimension $p_2 \times p_2$. Then, DRAGON assigns significance levels to partial correlations using the following steps:

- (i) Simulate data under the null hypotheses ($H_0 : \rho = 0$) for given sample size n , and estimate corresponding partial correlations using Dragon with λ_1 and λ_2 given from the original data.
- (ii) Fit κ using MLE of Eq. (10) for $P^{(1,1)}$, $P^{(1,2)}$, and $P^{(2,2)}$, separately.
- (iii) Use density Eq. (10) with κ determined in (ii) to assign significance levels to $\hat{P}^{(1,1)}$, $\hat{P}^{(1,2)}$, $\hat{P}^{(2,2)}$, respectively.
- (iv) Adjust significance levels in layer (1,1), (1,2), and (2,2) for multiple testing, separately, using the method of Benjamini and Hochberg [22]. Note, if we control the false discovery rate (FDR) at level α in each layer, we also control the overall FDR at level α across all layers. However, p_1 and p_2 are assumed to be sufficiently large.

For $n \gg p$, κ is given by $\kappa = n - 1 - (p - 2)$ and (i – ii) are not necessary.

2.4 Standard Gaussian Graphical Model implementation

A multitude of methods exist to estimate GGMs, all of which have pros and cons [7]. For better comparability, we focus on the so-called covariance shrinkage approach, which is a widely used method for GGM estimation [12, 23]. This approach is most suited for a comparison to DRAGON, since DRAGON is an extension of its basic concepts.

The R-package “GeneNet” [23] assesses the significance of edges using a mixture model. However, as thoroughly shown in [21], a more proper way is to use the exact null distribution for shrunken partial correlations. Thus, we also use this latter approach for our implementation of the GGM, which we simply refer to as “GGM” throughout the article.

3 Results and Discussion

3.1 Simulation studies

The simulation studies were performed using fixed numbers of features $p_1 = 100$ and $p_2 = 500$ for omics layer 1 and 2, respectively. In each of studies A , B , C , and D we varied the percentage of entries, $\eta^{(k,l)}$, in the precision matrices $\hat{\Theta}^{(k,l)}$, as summarized in Table 1, which also shows the corresponding numbers of edges. The precision matrices were generated as follows:

- (0) start with a p dimensional identity matrix, where $p = p_1 + p_2$,
- (1) randomly replace a proportion $\eta^{(k,l)}$ of zeros by values drawn from a uniform distribution ranging from -1 to 1 ,
- (2) replace the diagonal entries θ_{ii} by $\sum_j |\theta_{ij}|$ plus a small positive value ($\epsilon = 0.0001$),
- (3) normalize the entries θ_{ij} of the precision matrix by $\sqrt{\theta_{ii}\theta_{jj}}$.

This precision matrix was used to draw n samples from a multivariate normal with mean vector $\mu = 0$ and covariance $\hat{\Theta}^{-1}$. Finally, we added a noise $\epsilon \sim N(\mu = 0, \sigma = 0.1)$ to each entry of the data matrix.

Table 1: Edge densities and edge numbers for simulation studies A , B , C , and D .

(k, l)	(1, 1)		(1, 2)		(2, 2)	
	η	edges	η	edges	η	edges
A	0.05	248	0.05	2500	0.05	6238
B	0.05	248	0.05	2500	0.005	624
C	0.05	248	0.005	250	0.005	624
D	0.101	500	0.01	500	0.004	500

3.1.1 DRAGON adapts to the data by dynamically chosen penalty parameters

DRAGON uses an analytical estimate of the minimum of R , Eq. (6). Here, we illustrate that this estimate dynamically adapts to sample and feature size, and to edge densities $\eta^{(k,l)}$. First, we consider simulation study A , where we have equal edge densities $\eta^{(1,1)} = \eta^{(1,2)} = \eta^{(2,2)} = 0.05$. Figures 1a and c show R in dependency of λ_1 and λ_2 for the analytical estimate and the ground truth, respectively, for a fixed sample size of $n = 5000$. First, we observed that estimate and ground truth agree remarkably well, and that they provide almost identical estimates for the position of the minimum of the selected penalty parameters, $(\hat{\lambda}_1, \hat{\lambda}_2)$. Note, the GGM Eq. (2) using the appended data $X = [X^{(1)}, X^{(2)}]$ corresponds to the diagonal red lines, i.e. the two data layers are treated as they would belong to one layer and a single regularization parameter $\lambda_1 = \lambda_2 = \lambda$ is estimated. We observed that DRAGON correctly estimated $(\hat{\lambda}_1, \hat{\lambda}_2)$ to be near to the diagonal for this simulation study. Supplementary Figures S1 and S2 confirm this finding for lower sample sizes, $n = 500$ and $n = 1000$, respectively.

Next, we investigated the influence of the edge densities $\eta^{(k,l)}$ on R . For this, we reduced in simulation study B the edge density $\eta^{(2,2)}$ to $\eta^{(2,2)} = 0.005$. Again, we observed a remarkable agreement between estimated and true R , shown in Figure 1b and d, respectively, which is also the case for the estimated minima $(\hat{\lambda}_1, \hat{\lambda}_2)$. Note, $\hat{\lambda}_1$ now strongly differs from $\hat{\lambda}_2$. Since $\lambda_2 > \lambda_1$, the second omics data layer is stronger penalized than the first. We repeated this analysis for two further simulation studies, C and D , which both have unbalanced edge densities with results shown in supplementary Figure S3, S4, and S5 for $n = 500$, $n = 1000$, and $n = 5000$, respectively. Here, we also observed that DRAGON, first, correctly estimates R and, second, that λ_1 and λ_2 are chosen accordingly to minimize R .

3.1.2 DRAGON improves model inference

We assessed the performance for model inference by evaluating the log-likelihood for DRAGON and the GGM on $n = 1,000$ test samples. For this, we repeated simulation studies A to D in total 100 times for different sample sizes n with results shown in Figure S6. We observed similar results on an absolute scale, Figures S6a to d, but results were clearly in favor of DRAGON when we evaluated the log-likelihood difference, Figures S6e to h. This paired measure has the advantage that we remove variability due to different simulation runs. The green line corresponds to the median log-likelihood difference and the error bands to the 25% and 75% percentiles. Results were slightly in favor of the GGM for the balanced study A . In studies B , C , and D , DRAGON outperformed the standard GGM, as indicated by positive values. Strongest improvements were observed for the unbalanced simulation B . Note, for very large sample sizes, DRAGON and GGM coincide, as also verified by a vanishing log-likelihood difference.

3.1.3 DRAGON improves edge recovery

Adjusted p -values were assigned as described in the Materials and Methods section for DRAGON and the GGM, respectively, and were used to assess the edge-recovery performance in simulation studies A to D using receiver operating characteristic (ROC) curves.

Figure 2a shows the area under the ROC curve (AUC) in dependence of the number of training samples n for simulation study A . In this study, we observed almost identical performance for DRAGON and GGM for all considered sample sizes, which is in accordance with our previous findings. For simulation studies B , C , and D , the corresponding results are shown in Figures 2b to d. Here, we observed substantial improvements for DRAGON compared to GGM. For instance, in simulation study D , DRAGON achieved a AUC for $n \approx 200$ samples that is compatible to that of the GGM for $n \approx 1000$ samples. This is further substantiated by Figures 2e to h, that show the respective AUC differences. Here, we

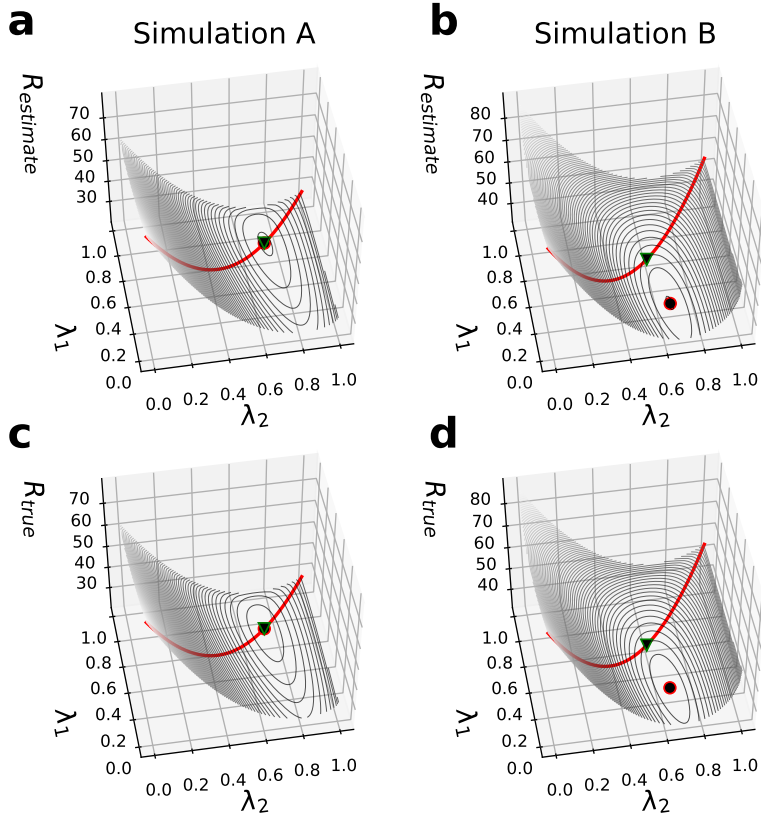


Figure 1: Parameter landscapes for DRAGON. Estimated and true R (upper and lower row) in dependency of λ_1 and λ_2 in simulation studies A (left column) and B (right column). Figures a and b show the estimated R for study A and B , respectively. Figure c and d show the corresponding ground truth. The red circles indicate the minima for each plot in the λ_1 – λ_2 plane, and the green triangles give the minima on the diagonal R values shown in red, corresponding to the standard GGM.

observed AUC improvements up to ~ 0.14 (study B), ~ 0.05 (study C) and ~ 0.13 (study D). Only for the balanced simulation scenario A , the GGM negligibly outperformed DRAGON, as shown by small negative values in Figure 2e. For an alternative performance assessment, we used the average area under the precision-recall curve (AUC-PR). Results are shown in Supplementary Figures S7a to h. Also here, results are clearly in favor of DRAGON.

We also verified that DRAGON correctly estimates p -values and false discovery rates (FDRs). First, we performed simulations under the null hypothesis ($\rho = 0$), and verified that the p -value distributions are flat for different sets of the regularization parameters λ_1 and λ_2 (Figures S10 - 11). The investigated sets were motivated as follows: we recorded the λ_1 and λ_2 values for each simulation run in study A to D , which yielded the results shown in Figure S10. Then, we extracted the corresponding parameter sets at $n = 256$, $n = 1024$ and $n = 4096$ samples, which corresponds to a highly regularized estimate, a moderately regularized one, and one with low regularization, respectively. This resulted in total in 12 pairs (λ_1, λ_2) with the respective p -value distributions under the null hypothesis shown in Figure S11. Moreover, we recorded the FDRs corresponding to studies A to D with results shown in Figures S8 and S9 for the empirical estimate of κ and the theoretical value $\kappa = n - 1 - (p - 2)$, respectively.

3.2 Analysis of joint transcriptome–epitope data in single cord blood mononuclear cells

Single-cell RNA-sequencing raw counts of 8,618 cord blood mononuclear cells (CBMC) together with corresponding centered log-ratio (CLR) transformed protein levels of cell-surface markers (the epitopes)

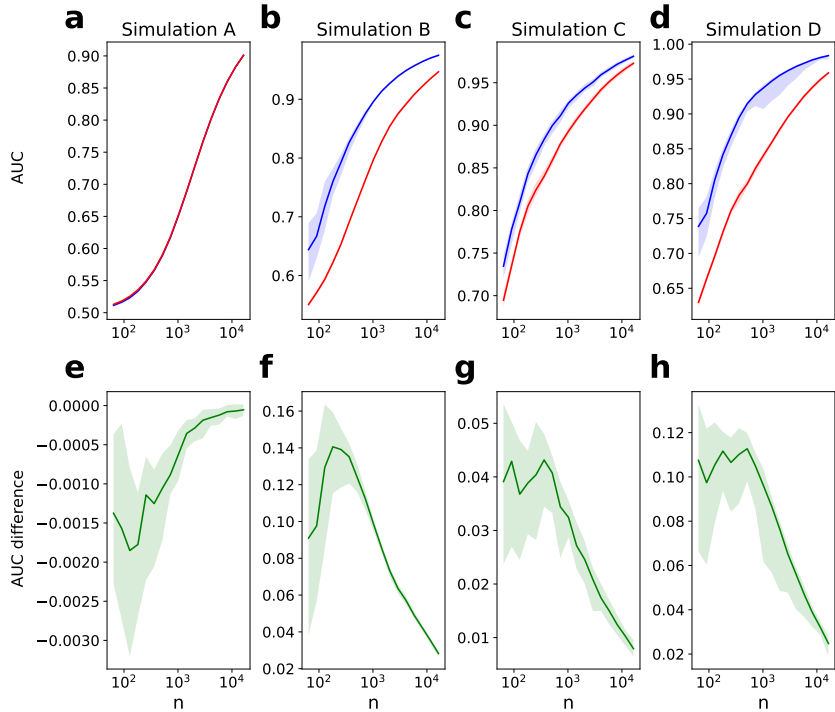


Figure 2: Area under the ROC curve (AUC) for DRAGON and GGM. The upper row, Figures a to d give the AUC evaluated on test data versus the number of training samples, n , for simulation studies *A* to *D*, respectively. Results from DRAGON are given in blue and those from the GGM in red. The lines correspond to the median AUC and the bands to the 25% and 75% percentiles of the distribution. Figures e to h show the corresponding AUC differences (DRAGON minus GGM) in green.

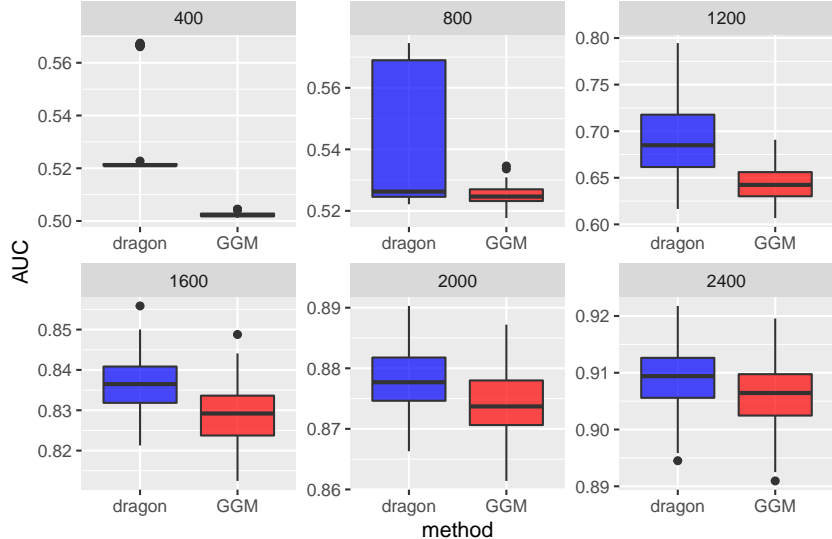


Figure 3: ROC AUC comparison between DRAGON and the GGM using joint transcriptome–epitope single-cell data from [24]. Here, boxplots of AUCs were obtained from 100 subsampling runs for the different sample sizes indicated at the top of each plot. Blue boxplots correspond to DRAGON and those in red to the GGM.

[24] (GSE100866) were downloaded from <https://www.ncbi.nlm.nih.gov/geo/>. The RNA-sequencing data were processed by (i) scaling to an equal library size (chosen as the mean library size across all cells), (ii) by adding a pseudo count, (iii) by \log_2 transforming the data, and (iv) by performing a nonparanormal transformation using the function “huge.npn” with standard settings, provided in the R package “huge” [25]. The latter step was performed to deal with non-normal data. Note that the independence relations among the variables are still encoded in the precision matrix if a nonparanormal transformation is performed [26]. The dataset consists of single cells from both human and mice. The latter were identified and removed from the dataset using hierarchical clustering on the ten highest expressed human genes together with the ten highest expressed mouse genes (Figure S12). The final dataset included 8,007 single cell profiles.

In [24], CITE-seq was proposed to combine highly multiplexed protein marker detection with unbiased transcriptome profiling in single cells. The CBMC transcriptomes were measured simultaneously in the same cells with 13 cell-surface markers: CD3, CD4, CD8, CD45RA, CD56, CD16, CD10, CD11c, CD14, CD19, CD34, CCR5, CCR7. We combined these data with the 500 most abundant human RNAs, which was necessary to allow for a fair comparison between DRAGON and the GGM: both methods become almost identical if n is sufficiently large compared to p (here, the regularization becomes negligible). This allowed us to define a ground truth based on the 8,007 human cells, where we estimated partial correlations using the GGM with vanishing regularization ($\lambda = 0$) and defined an edge by an $\text{FDR} < 0.05$.

As in simulation studies *A* to *D*, we compared DRAGON, which explicitly takes into account that the data comprises two different data modalities, with the GGM, which treats both omics layers as if they would belong to the same layer. We repeatedly sampled training data for different sample sizes ranging from $n = 400$ to $n = 2,400$ together with $n = 1,000$ test samples. For each of these sampling runs, we recorded the log-likelihood on the test data shown in Figure S13 and calculated the difference between DRAGON and GGM with results shown in Figure 4. Here, we obtained thoroughly positive values across all 100 subsampling runs, which corresponds to better estimates of the joint distribution for DRAGON compared to the GGM.

Next, we investigated the edge-recovery performance using the ground truth as described above. This yielded the corresponding areas under the ROC curve as shown in Figure 3. We additionally evaluated the average area under the precision-recall curve with results shown in Figure S14. For both measures, DRAGON outcompeted the GGM, with strongest improvements seen for low to moderate sample sizes. For sample sizes $n = 2,000$ and $n = 2,400$ both performed similar.

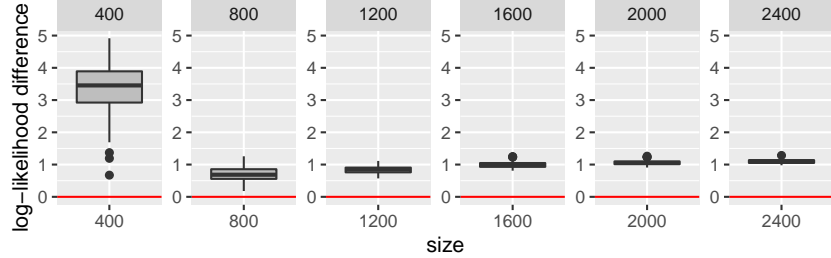


Figure 4: Log-likelihood differences between DRAGON and the GGM using joint transcriptome–epitope single-cell data from [24]. Here, boxplots show the log-likelihood difference calculated for DRAGON minus that from the GGM obtained from 100 subsampling runs. The log-likelihood differences were evaluated on 1,000 single-cell profiles which were not included in the training step. As in Figure 3, the different figures correspond to different sample sizes as indicated at the top of the plots. The red lines indicate a log-likelihood difference of zero.

3.3 Analysis of joint transcriptome–methylation data from breast cancer specimens

Pre-processed breast cancer gene expression and methylation data from The Cancer Genome Atlas (TCGA) [27], available from TCGA2BED [28], was downloaded from <http://bioinf.iasi.cnr.it/tcga2bed/> on 01/12/2020. A combined gene expression and methylation matrix was constructed using the TCGA2BED provided software available from <http://bioinf.iasi.cnr.it/genint/>. RNA-seq expression data were filtered to remove genes with consistently low expression, defined as genes having an expression value < 1 in $> 20\%$ of the samples. Methylation data were filtered to remove genes with missing (NA) methylation values. Expression and methylation data were then scaled to have mean 0 and standard deviation 1. A demonstration set of 667 transcription factors (TFs) was selected (Supplementary Dataset 1) and the GGM was run on the expression values for these TFs, and DRAGON was applied to the expression and methylation values measured for these TFs.

We used DRAGON to calculate the associations between 667 transcription factors across expression and methylation data in breast cancer to explore the regulatory relationships that these transcription factors have with each other. In the TCGA breast cancer data, 872 samples had both RNA-seq and DNA-methylation data available. For our application, we limited the set of genes to characterized transcription factors with motif information, allowing us to demonstrate the utility of this method on a reasonable number of variables given the available sample size.

Figure 5 shows the network of significant associations at adjusted p -value ≤ 0.05 , with expression-expression associations shown as blue edges, methylation-methylation associations shown as yellow edges and expression-methylation associations shown as purple edges.

The most significant edges between expression and methylation data are associations between the methylation levels of a gene and the expression levels of the same gene, as evident by the pink “self loops” in the network in Figure 5. However, this is exactly what one should have expected. DNA methylation exerts its effects locally, altering the expression of the methylated gene; secondary effects can occur in the alteration of expression of other genes, but these are mediated by multiple factors in the cell that generally work together to maintain homeostasis.

DRAGON isolates possible origins of associations DRAGON allows one to calculate associations between genes based on multiple data types. DRAGON also removes redundant information from associations in one data type, that can be explained by associations with another data type. An example of this can be seen in the associations between the transcription factors ELF4 and ZBTB33 (Table 2). When estimating a GGM using only gene expression data, ELF4 and ZBTB33 have a significant partial correlation, indicating the co-expression of these genes at a significance level of adjusted p -value ≤ 0.05 . When performing a DRAGON analysis using both gene expression and gene DNA methylation data, we see that the partial correlation between the gene expression levels of ELF4 and ZBTB33 is reduced, and no longer significant at a level of adjusted p -value ≤ 0.05 . However, we do see that the methyla-

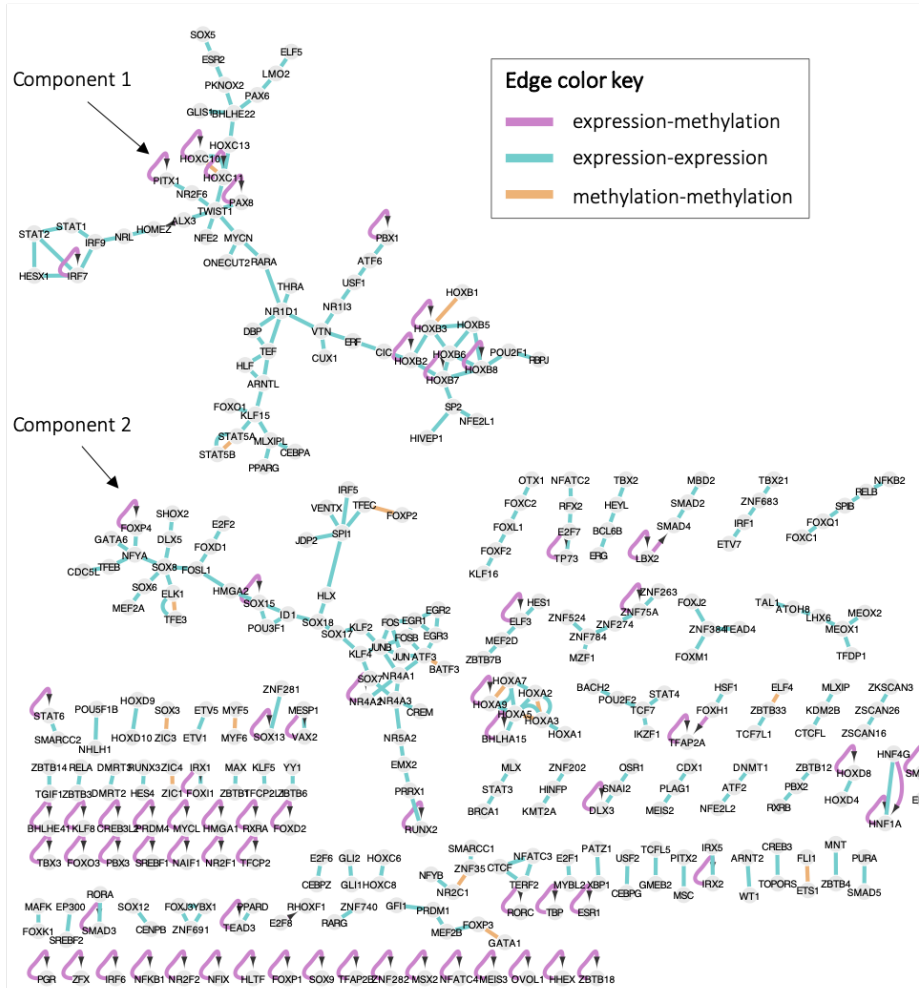


Figure 5: Network view of all significant (adjusted p -value ≤ 0.05) associations when performing a DRAGON analysis on gene methylation and expression data for 667 transcription factors in breast cancer. Visualized in Cytoscape [29]

Table 2: Partial correlations between ELF4 and ZBTB33 for the GGM vs DRAGON.

Edge type	Adj. p-val.	Partial Cor
expr.-expr. (GGM)	0.002	0.189
expr.-expr. (DRAGON)	0.059	0.115
methyl.-methyl. (DRAGON)	0.017	0.216

tion levels of ELF4 and ZBTB33 have a significant partial correlation in the DRAGON analysis. Thus, using DRAGON allows us to see that while the expression of two genes are correlated, this observed co-expression can be explained by their methylation levels, providing us insight into the mechanism of regulation of these two transcription factors – they are co-expressed because they are co-methylated.

DRAGON identifies meaningful spatial connections Topologically associated domains (TADs) are sections of DNA that are self-interacting, meaning that elements within a TAD tend to interact with elements in the same TAD rather than elsewhere in the genome. Chromosome conformation capture techniques such as Hi-C allow one to detect both local TADs [30] as well as long range interactions [31], providing insight into the 3D organization of the genome. DRAGON associations, particularly those involving methylation signals, reveal both short-range and long-range interactions.

3.3.1 Short range connections – Topologically Associated Domains

Significant methylation-methylation edges tend to be closer to each other in terms of chromosome coordinates compared to non-significant methylation-methylation edges. Figure S12 shows the inter-gene distances for significant methylation-methylation edges vs non-significant edges for TFs on the same chromosome, illustrating the closer proximity of significant methylation-methylation edges.

For inter-chromosomal methylation-methylation edges, only 1 of 16 significant methylation-methylation edges link genes on separate chromosomes (meaning 15 of 16 significant edges link genes on the same chromosome), whereas nearly all (207,307 of 218,775, or 95%) non-significant edges link genes that are on separate chromosomes.

A specific example can be seen in Figure 6, where a cluster of HOXA genes have significant methylation-methylation, expression-expression, and expression-methylation edges. Investigating the positions of these genes in the genome, one can see that they are all adjacent to each other. Hi-C data in GM12878 (Figure 6, as well as K562 (Supplementary Figure S16) indicate that these genes are within the same self-associating TAD.

3.3.2 Long range connections – DNA loops

In addition to short-range interactions, a significant DRAGON association can also indicate a potential long-range DNA interaction. Hi-C data in the 3D Genome Browser [32] indicates a potential 3D DNA loop interaction between ZBTB33 and ELF4, two genes that have a significant methylation-methylation association. Figure 7 shows a heatmap of the Hi-C interactions for pairs of loci on the *x*-axis. ZBTB33 and ELF4 have a Hi-C signal indicating their physical interaction. In addition, ELF4 and ZBTB are not within the same TAD, and are ~10 Mb apart, suggesting that these loci may be interacting via a DNA loop.

DRAGON network neighborhoods show functional enrichment Gene Ontology (GO) term enrichment analysis of gene sets in neighborhoods of DRAGON networks show significant functional enrichment in different GO terms. GO enrichment analysis was performed on the gene sets indicated in Figure 8, and identified various biological process functional enrichment in each of the gene sets (Supplementary Tables S1-S5, Supplementary Figures S2-S6, Supplementary Tables S17-S21). This suggests that DRAGON associations are connecting genes that are involved in similar/related functions.

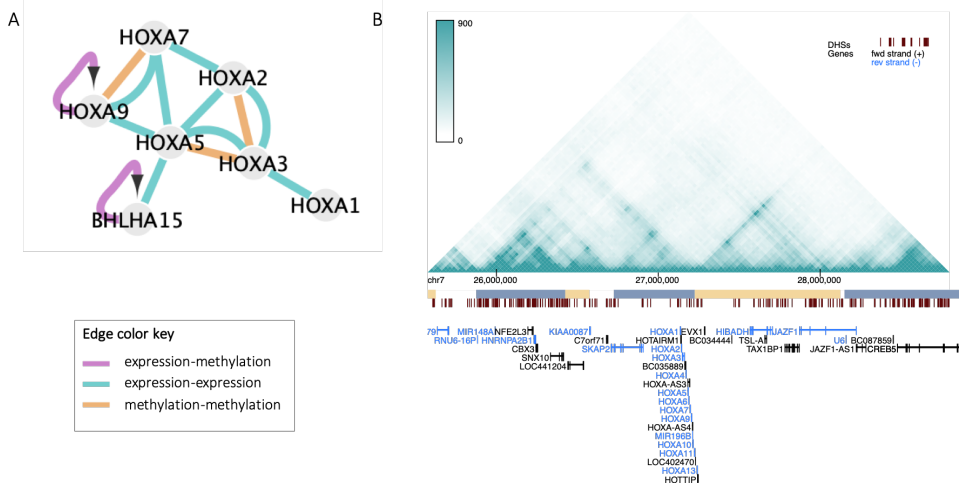


Figure 6: A subnetwork of HOXA genes that are located within the same TAD on chromosome 7 in Hi-C data of the cell line GM12878, as indicated by the blue bar. Hi-C data and plots accessed from the 3D Genome Browser [32]. Blue and yellow bars indicate TADs.

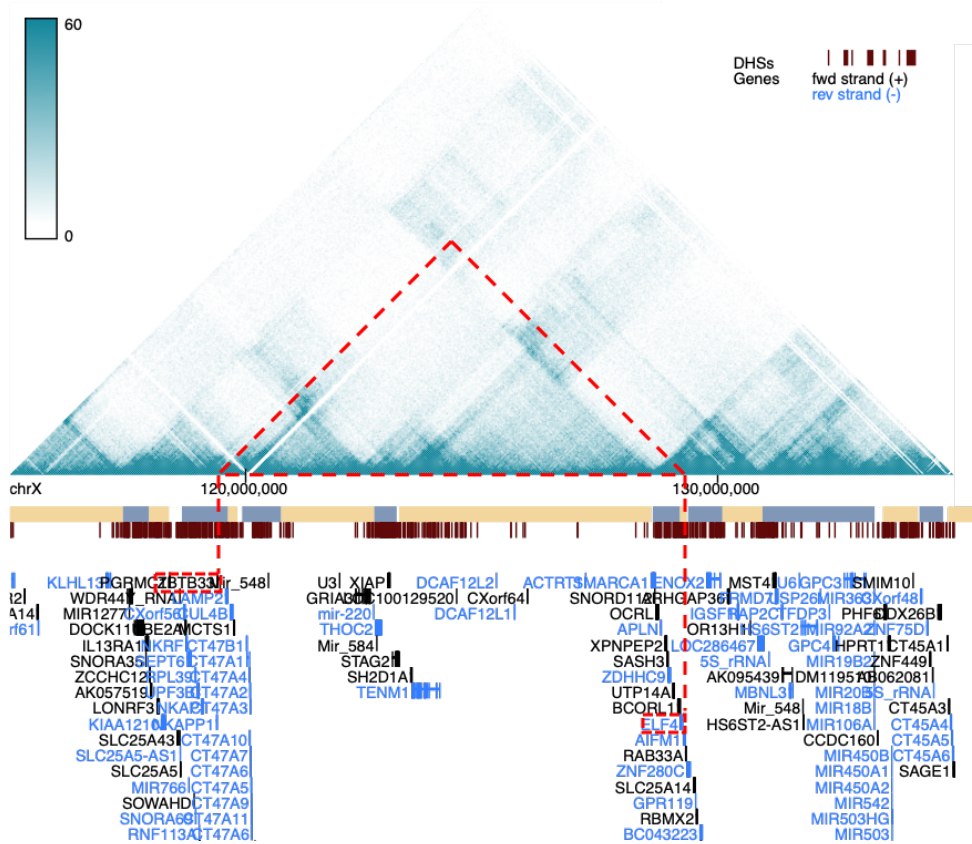


Figure 7: Heatmap of Hi-C data indicating a potential physical interaction between ELF4 and ZBTB33 via a DNA loop. The heatmap shows the Hi-C interaction quantification for pairs of loci on the x-axis. Figure generated using the 3D Genome Browser [32]. Red lines added to indicate the two genes of interest.

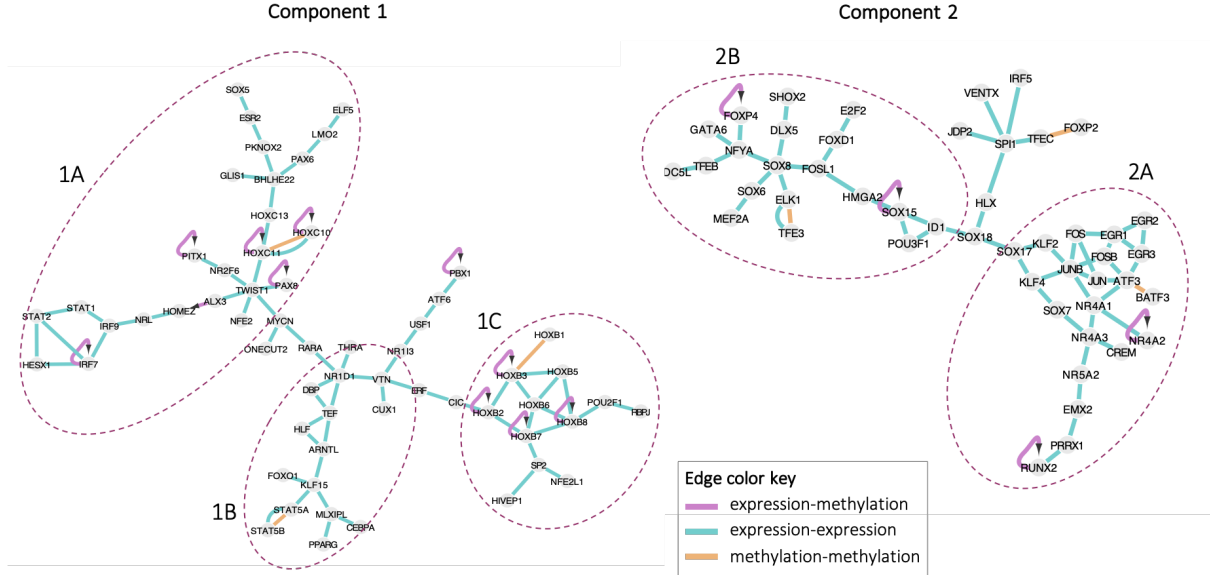


Figure 8: Gene sets within neighborhoods of the network of significant DRAGON associations.

4 Conclusion and Summary

DRAGON allows integration of multiple layers of omics data into a unified association network that allows us to understand both associations between biological variables such as gene expression and the potential drivers of the observed correlations. DRAGON is based on Gaussian Graphical Models and uses a regularization scheme to optimize the trade-off between the network’s complexity and its estimation accuracy, while explicitly taking into account the data modalities of the assessed omics layers. DRAGON accounts for differences in edge densities and feature sizes, enabling an enhanced estimation of partial correlations compared to layer-agnostic GGMs. This is particularly true if the number of variables is the same order of magnitude or exceeds the sample size (as is the case in nearly all omics experiments).

We used DRAGON to analyze joint transcriptome-methylation data obtained from breast cancer specimens. The addition of methylation data to transcription factor gene expression allowed DRAGON to identify putative regulatory mechanisms, finding consistent associations between co-expression and co-methylation. This indicates that for many transcription factors its own methylation signal is a strong independent regulator of its expression. Further, analysis using DRAGON also allowed identification of possible regulatory effects driven by the spatial organization of the genome.

We recognize that DRAGON has some limitations. DRAGON is based on Gaussian graphical modeling and so it assumes multivariate normally distributed data. For biological data, this normality assumption generally does not hold so we introduced data transformations to make both the methylation and the RNA-sequencing data approximately normally distributed; this allowed us to use DRAGON with these data sets. However, other data types, such as single-nucleotide polymorphisms (SNPs), are categorical, and as such alternative methods are needed; extending our method to Mixed Graphical Models [33, 34] could be a possible solution. Despite these limitations, DRAGON represents a significant step forward that improves the modeling of partial correlations across multiple layers of omics data and provides new insights into regulatory processes that may be missed by other methods.

5 Code and data availability

DRAGON is available through the Network Zoo package (netZooPy v0.8; netzoo.github.io). A Jupyter notebook to reproduce the analysis is available in netBooks (netbooks.networkmedicine.org).

6 Support

DW, RB, MBG, JQ, and MA were supported by grants from the US National Cancer Institute (1R35CA220523 and 1U24CA231846). The work of HUZ and MA was supported by the German Federal Ministry of Education and Research (BMBF) within the framework of the e:Med research and funding concept (grant no. 01ZX1912A and 01ZX1912C).

References

- [1] Ulrich Stelzl, Uwe Worm, Maciej Lalowski, Christian Haenig, Felix H Brembeck, Heike Goehler, Martin Stroedicke, Martina Zenkner, Anke Schoenherr, Susanne Koeppen, et al. A human protein–protein interaction network: a resource for annotating the proteome. *Cell*, 122(6):957–968, 2005.
- [2] Jean-François Rual, Kavitha Venkatesan, Tong Hao, Tomoko Hirozane-Kishikawa, Amélie Dricot, Ning Li, Gabriel F Berriz, Francis D Gibbons, Matija Dreze, Nono Ayivi-Guedehoussou, et al. Towards a proteome-scale map of the human protein–protein interaction network. *Nature*, 437(7062):1173–1178, 2005.
- [3] Damian Szkłarczyk, Annika L Gable, David Lyon, Alexander Junge, Stefan Wyder, Jaime Huerta-Cepas, Milan Simonovic, Nadezhda T Doncheva, John H Morris, Peer Bork, et al. String v11: protein–protein association networks with increased coverage, supporting functional discovery in genome-wide experimental datasets. *Nucleic acids research*, 47(D1):D607–D613, 2019.
- [4] Florian Markowetz and Rainer Spang. Inferring cellular networks—a review. *BMC bioinformatics*, 8(6):S5, 2007.
- [5] Kimberly Glass, Curtis Huttenhower, John Quackenbush, and Guo-Cheng Yuan. Passing messages between biological networks to refine predicted interactions. *PloS one*, 8(5), 2013.
- [6] Koh Aoki, Yoshiyuki Ogata, and Daisuke Shibata. Approaches for extracting practical information from gene co-expression networks in plant biology. *Plant and Cell Physiology*, 48(3):381–390, 2007.
- [7] Michael Altenbuchinger, Antoine Weihs, John Quackenbush, Hans Jörgen Grabe, and Helena U Zacharias. Gaussian and mixed graphical models as (multi-) omics data analysis tools. *Biochimica et Biophysica Acta (BBA)-Gene Regulatory Mechanisms*, 1863(6):194418, 2020.
- [8] John Aldrich et al. Correlations genuine and spurious in pearson and yule. *Statistical science*, 10(4):364–376, 1995.
- [9] Adam A Margolin, Ilya Nemenman, Katia Basso, Chris Wiggins, Gustavo Stolovitzky, Riccardo Dalla Favera, and Andrea Califano. Aracne: an algorithm for the reconstruction of gene regulatory networks in a mammalian cellular context. In *BMC bioinformatics*, volume 7, page S7. Springer, 2006.
- [10] Atul J Butte and Isaac S Kohane. Mutual information relevance networks: functional genomic clustering using pairwise entropy measurements. In *Biocomputing 2000*, pages 418–429. World Scientific, 1999.
- [11] Anja Wille, Philip Zimmermann, Eva Vranová, Andreas Fürholz, Oliver Laule, Stefan Bleuler, Lars Hennig, Amela Prelić, Peter von Rohr, Lothar Thiele, et al. Sparse graphical gaussian modeling of the isoprenoid gene network in *arabidopsis thaliana*. *Genome biology*, 5(11):R92, 2004.
- [12] Juliane Schäfer and Korbinian Strimmer. A shrinkage approach to large-scale covariance matrix estimation and implications for functional genomics. *Statistical applications in genetics and molecular biology*, 4(1), 2005.
- [13] Jan Krumsiek, Karsten Suhre, Thomas Illig, Jerzy Adamski, and Fabian J Theis. Gaussian graphical modeling reconstructs pathway reactions from high-throughput metabolomics data. *BMC systems biology*, 5(1):21, 2011.

[14] Mahsa Ghanbari, Julia Lasserre, and Martin Vingron. The distance precision matrix: computing networks from non-linear relationships. *Bioinformatics*, 35(6):1009–1017, 2019.

[15] Junyue Cao, Darren A Cusanovich, Vijay Ramani, Delasa Aghamirzaie, Hannah A Pliner, Andrew J Hill, Riza M Daza, Jose L McFaline-Figueroa, Jonathan S Packer, Lena Christiansen, et al. Joint profiling of chromatin accessibility and gene expression in thousands of single cells. *Science*, 361(6409):1380–1385, 2018.

[16] Nicolai Meinshausen, Peter Bühlmann, et al. High-dimensional graphs and variable selection with the lasso. *The annals of statistics*, 34(3):1436–1462, 2006.

[17] Jerome Friedman, Trevor Hastie, and Robert Tibshirani. Sparse inverse covariance estimation with the graphical lasso. *Biostatistics*, 9(3):432–441, 2008.

[18] Steffen L Lauritzen. *Graphical models*, volume 17. Clarendon Press, 1996.

[19] Christopher M Bishop. *Pattern recognition and machine learning*. Springer, 2006.

[20] Olivier Ledoit and Michael Wolf. A well-conditioned estimator for large-dimensional covariance matrices. *Journal of multivariate analysis*, 88(2):365–411, 2004.

[21] Victor Bernal, Rainer Bischoff, Victor Guryev, Marco Grzegorczyk, and Peter Horvatovich. Exact hypothesis testing for shrinkage-based gaussian graphical models. *Bioinformatics*, 35(23):5011–5017, 2019.

[22] Yoav Benjamini and Yosef Hochberg. Controlling the false discovery rate: a practical and powerful approach to multiple testing. *Journal of the Royal statistical society: series B (Methodological)*, 57(1):289–300, 1995.

[23] Juliane Schaefer, Rainer Opgen-Rhein, and Korbinian Strimmer. *GeneNet: Modeling and Inferring Gene Networks*, 2020. R package version 1.2.15.

[24] Marlon Stoeckius, Christoph Hafemeister, William Stephenson, Brian Houck-Loomis, Pratip K Chattopadhyay, Harold Swerdlow, Rahul Satija, and Peter Smibert. Simultaneous epitope and transcriptome measurement in single cells. *Nature methods*, 14(9):865, 2017.

[25] Haoming Jiang, Xinyu Fei, Han Liu, Kathryn Roeder, John Lafferty, Larry Wasserman, Xingguo Li, and Tuo Zhao. *huge: High-Dimensional Undirected Graph Estimation*, 2020. R package version 1.3.4.1.

[26] Han Liu, John Lafferty, and Larry Wasserman. The nonparanormal: Semiparametric estimation of high dimensional undirected graphs. *Journal of Machine Learning Research*, 10(Oct):2295–2328, 2009.

[27] Katarzyna Tomczak, Patrycja Czerwińska, and Maciej Wiznerowicz. The cancer genome atlas (tcga): an immeasurable source of knowledge. *Contemporary oncology*, 19(1A):A68, 2015.

[28] Fabio Cumbo, Giulia Fiscon, Stefano Ceri, Marco Masseroli, and Emanuel Weitschek. Tcga2bed: extracting, extending, integrating, and querying the cancer genome atlas. *BMC bioinformatics*, 18(1):6, 2017.

[29] Paul Shannon, Andrew Markiel, Owen Ozier, Nitin S Baliga, Jonathan T Wang, Daniel Ramage, Nada Amin, Benno Schwikowski, and Trey Ideker. Cytoscape: a software environment for integrated models of biomolecular interaction networks. *Genome research*, 13(11):2498–2504, 2003.

[30] Quentin Szabo, Frédéric Bantignies, and Giacomo Cavalli. Principles of genome folding into topologically associating domains. *Science advances*, 5(4):eaaw1668, 2019.

[31] Erez Lieberman-Aiden, Nynke L Van Berkum, Louise Williams, Maxim Imakaev, Tobias Ragoczy, Agnes Telling, Ido Amit, Bryan R Lajoie, Peter J Sabo, Michael O Dorschner, et al. Comprehensive mapping of long-range interactions reveals folding principles of the human genome. *science*, 326(5950):289–293, 2009.

- [32] Yanli Wang, Fan Song, Bo Zhang, Lijun Zhang, Jie Xu, Da Kuang, Daofeng Li, Mayank NK Choudhary, Yun Li, Ming Hu, et al. The 3d genome browser: a web-based browser for visualizing 3d genome organization and long-range chromatin interactions. *Genome biology*, 19(1):1–12, 2018.
- [33] Jason D Lee and Trevor J Hastie. Learning the structure of mixed graphical models. *Journal of Computational and Graphical Statistics*, 24(1):230–253, 2015.
- [34] Michael Altenbuchinger, Helena U Zacharias, Stefan Solbrig, Andreas Schäfer, Mustafa Büyüközkan, Ulla T Schultheiß, Fruzsina Kotsis, Anna Köttgen, Rainer Spang, Peter J Oefner, et al. A multi-source data integration approach reveals novel associations between metabolites and renal outcomes in the german chronic kidney disease study. *Scientific reports*, 9(1):1–13, 2019.

Supplementary Material

*DRAGON: Determining Regulatory Associations using Graphical models on
multi-Omics Networks*

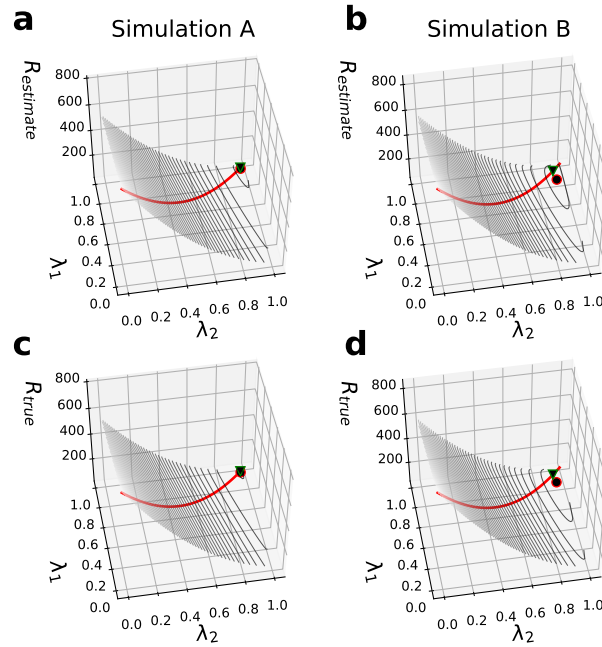


Figure S1: Parameter landscapes for DRAGON in studies *A* and *B*. The plot is understood analogous to Figure 1 in the main article but now for $n = 500$.

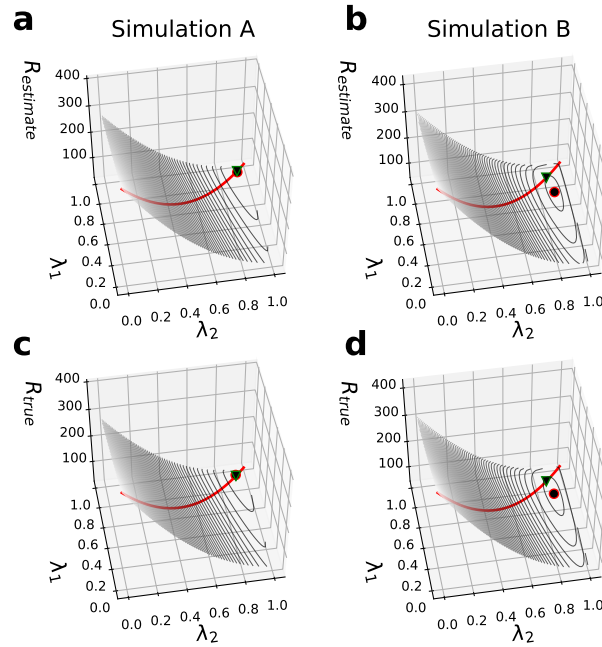


Figure S2: Parameter landscapes for DRAGON in studies *A* and *B*. The plot is understood analogous to Figure 1 in the main article but now for $n = 1,000$.

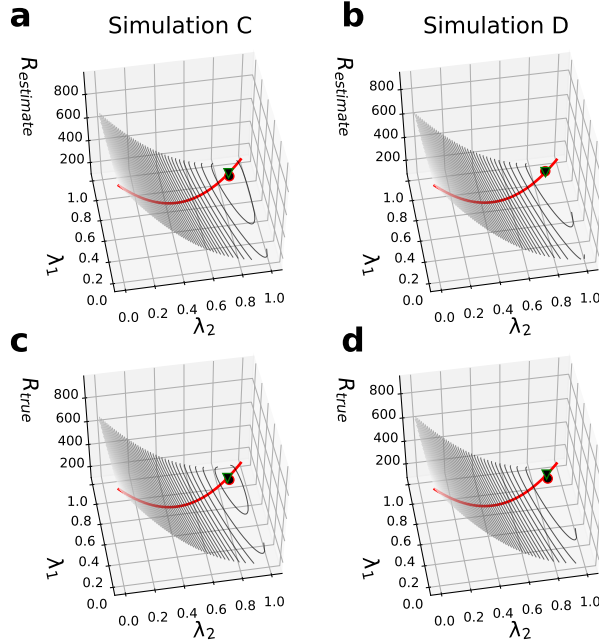


Figure S3: Parameter landscapes for DRAGON. Estimated and true R (upper and lower row) in dependency of λ_1 and λ_2 in simulation studies C (left column) and D (right column) for $n = 500$. Figures a and b show the estimated R for studies C and D , respectively. Figures c and d show the corresponding ground truth. The red circles indicate the minima for each plot in the λ_1 – λ_2 plane, and the green triangles give the minima on the diagonal R values shown in red, corresponding to the standard GGM.

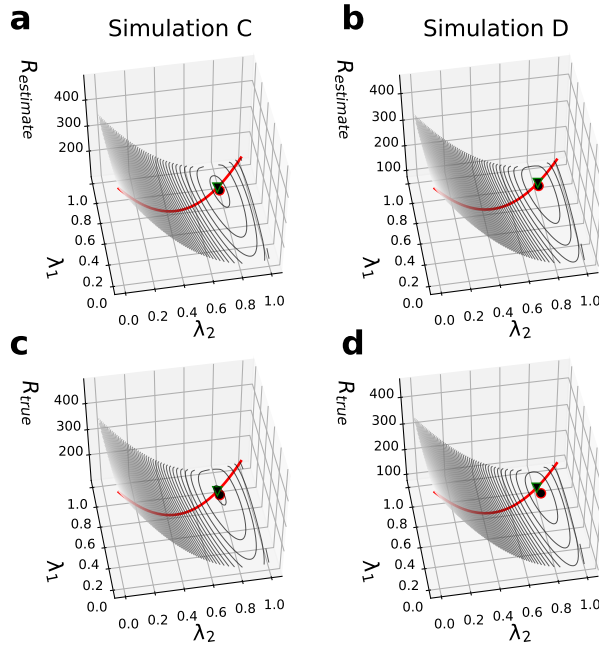


Figure S4: Parameter landscapes for DRAGON in studies C and D . The plot is understood analogous to Figure S5 but now for $n = 1,000$.

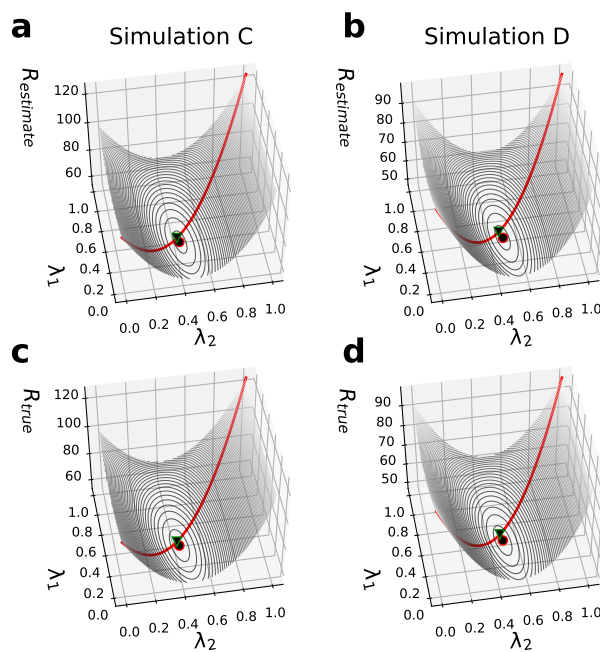


Figure S5: Parameter landscapes for DRAGON in studies *C* and *D*. The plot is understood analogous to Figure S5 but now for $n = 5,000$.

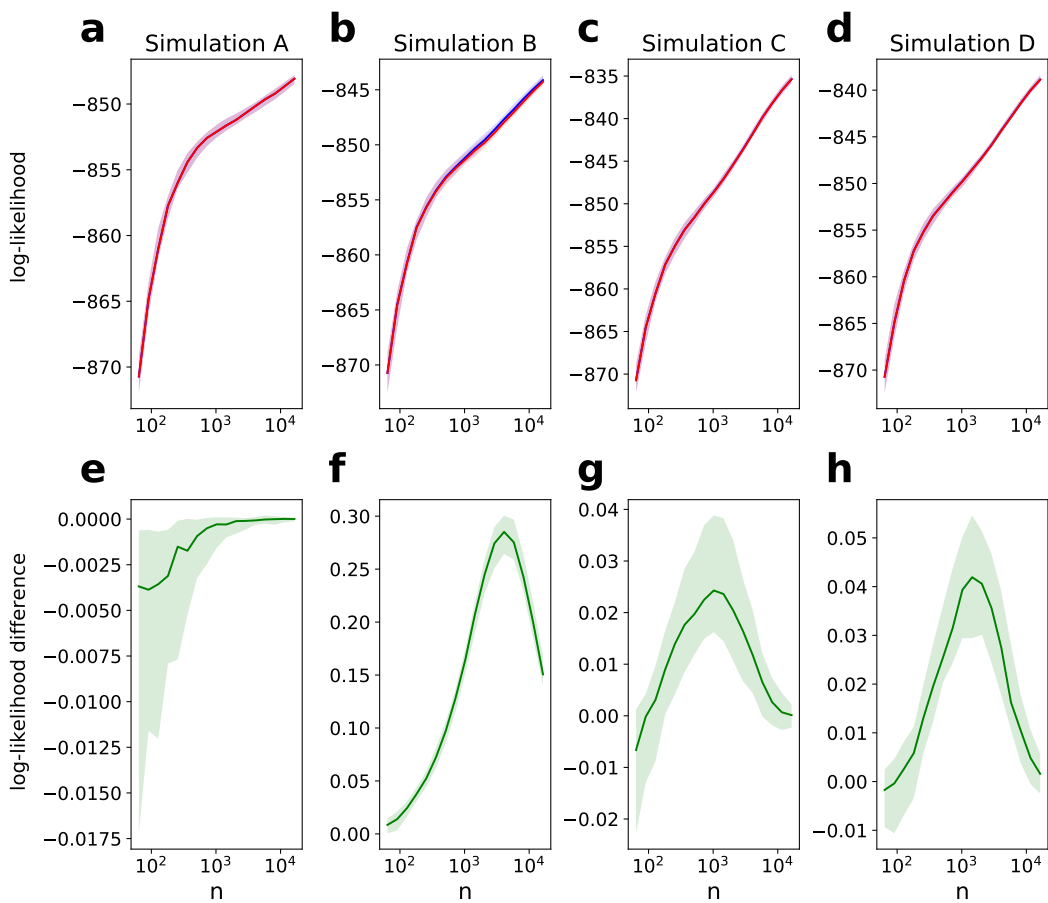


Figure S6: Log-likelihood comparison between DRAGON and GGM. The upper row, Figures a to d give the log-likelihood evaluated on test data versus the number of training samples, n , for simulation studies A to D, respectively. Results from DRAGON are given in blue and those from the GGM in red. The lines correspond to the median log-likelihood and the bands to the 25% and 75% percentiles of the distribution. Figures e to h show the corresponding log-likelihood differences (DRAGON minus GGM) in green.

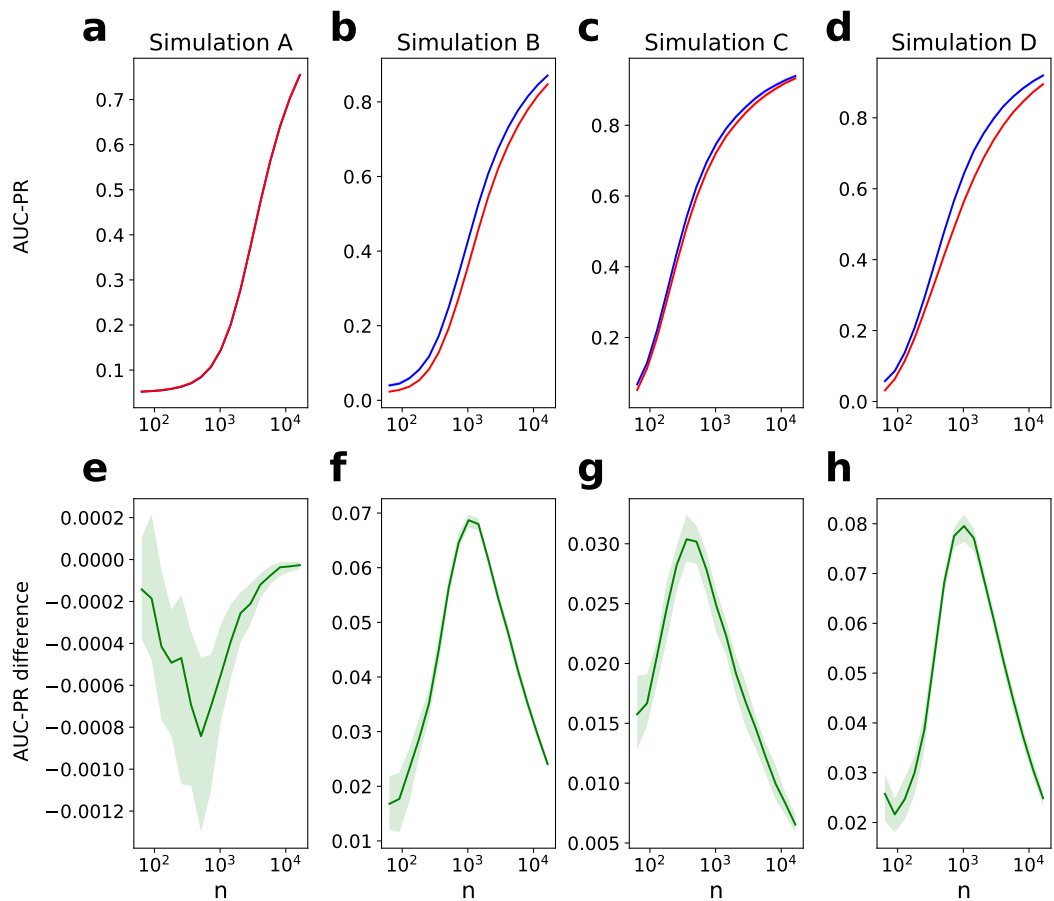


Figure S7: Comparison between DRAGON and GGM with respect to the area under the precision-recall curve (AUC-PR). The upper row, Figures a to d give the obtained AUC-PR versus the number of training samples, n , for simulation studies A to D, respectively. Results from DRAGON are given in blue and those from the GGM in red. The lines correspond to the median AUC-PR and the bands to the 25% and 75% percentiles of the distribution. Figures e to h show the corresponding AUC-PR differences (DRAGON minus GGM) in green.

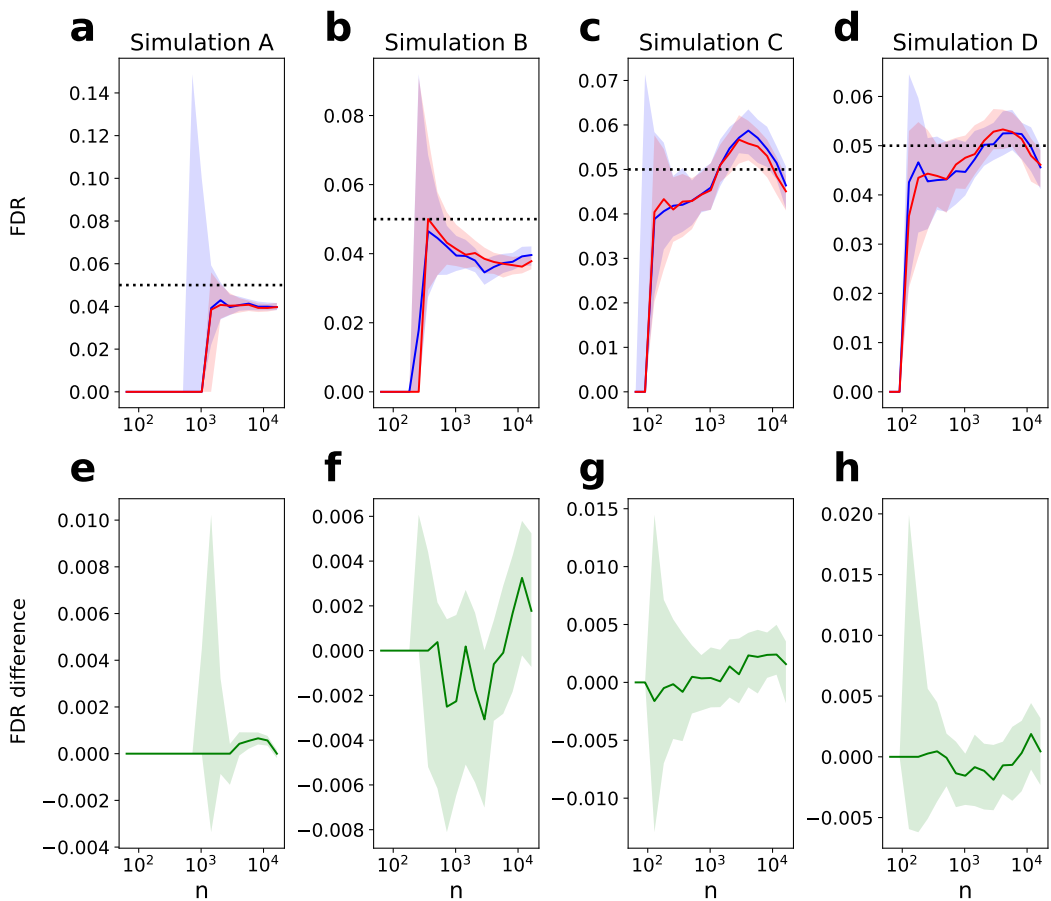


Figure S8: False-discovery rates (FDRs) for DRAGON and GGM in simulation studies. The upper row, Figures a to d give the observed FDRs versus the number of training samples, n , for simulation studies A to D, respectively. Results from DRAGON are given in blue and those from the GGM in red. The lines correspond to the median FDR and the bands to the 25% and 75% percentiles of the distribution. The dotted lines indicate the chosen significance threshold FDR = 0.05. Figures e to h show the corresponding FDR differences (DRAGON minus GGM) in green.

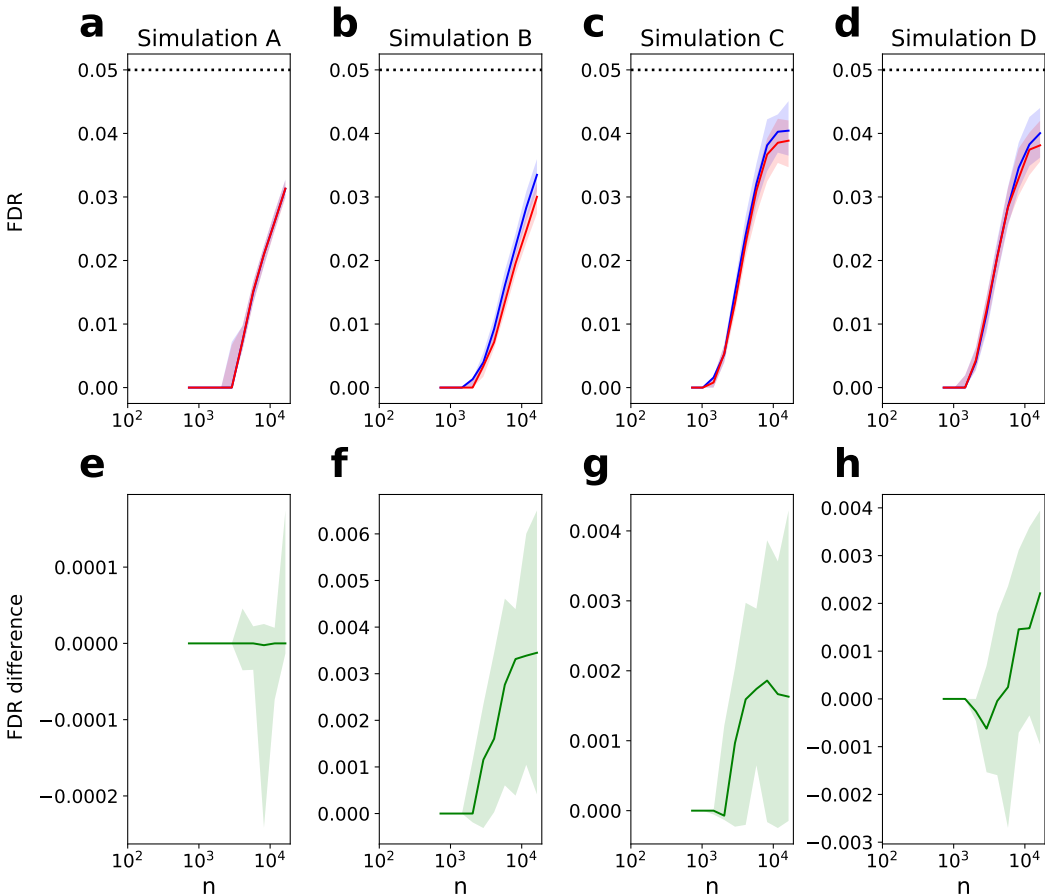


Figure S9: As Figure S8 but now using the theoretical value $\kappa = n - 1 - (p - 2)$ to estimate significance levels.

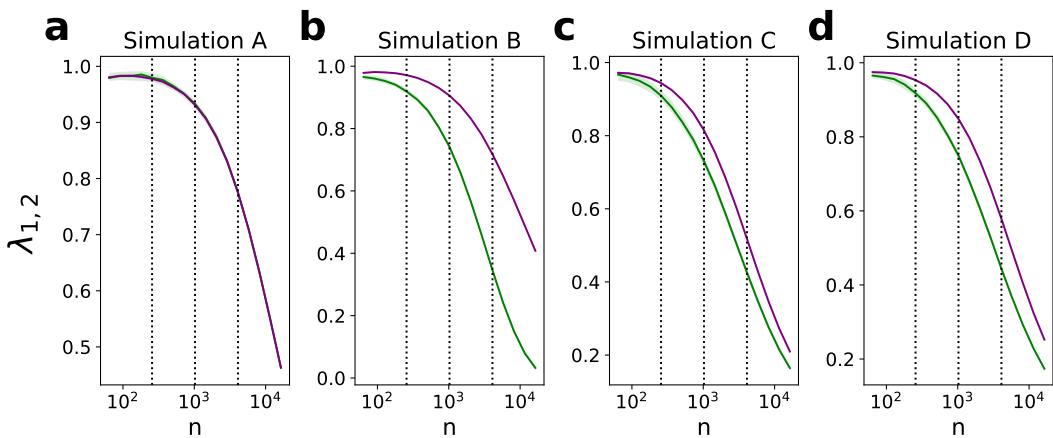


Figure S10: Regularization parameters λ_1 (green) and λ_2 (purple) for simulation studies A to D for different sample sizes. The vertical dotted lines correspond to $n = 256$, $n = 1,024$, and $n = 4,096$. The respective pairs (λ_1, λ_2) were evaluated to verify that p -value distributions are flat under the null hypothesis ($H_0 : \rho = 0$).

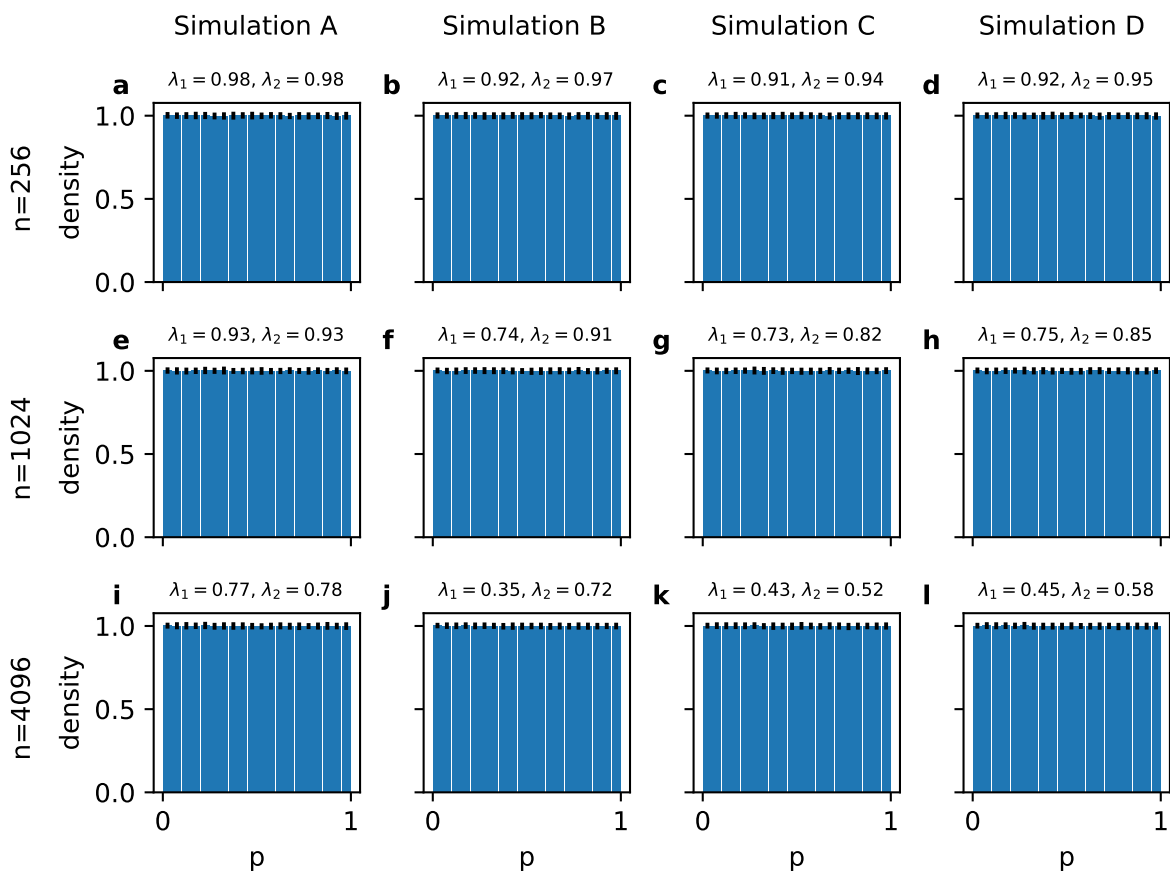


Figure S11: Distributions of p -values estimated by DRAGON for data simulated under the null hypothesis ($H_0 : p = 0$) for given pairs of the regularization parameters λ_1 and λ_2 . The (λ_1, λ_2) -pairs are given at the top of Figures a to l and were derived as described in the main article, cf. also Figure S10. Their corresponding sample size n and simulation study are given at the left side and at the top, respectively. Error bars represent ± 1 standard deviation across 10 simulation runs.

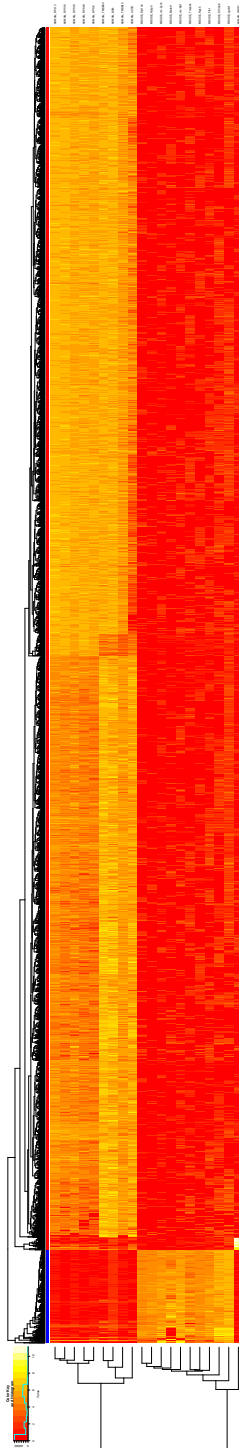


Figure S12: Heatmap with hierarchical clustering of human and mouse single-cell RNA sequencing profiles of 8,618 cord blood mononuclear cells (CBMC) downloaded from GEO with accession number GSE100866 [1]. We used the top ten highest expressed human and mouse genes for hierarchical clustering. The first cluster corresponds to mouse cells and were removed from subsequent analysis.

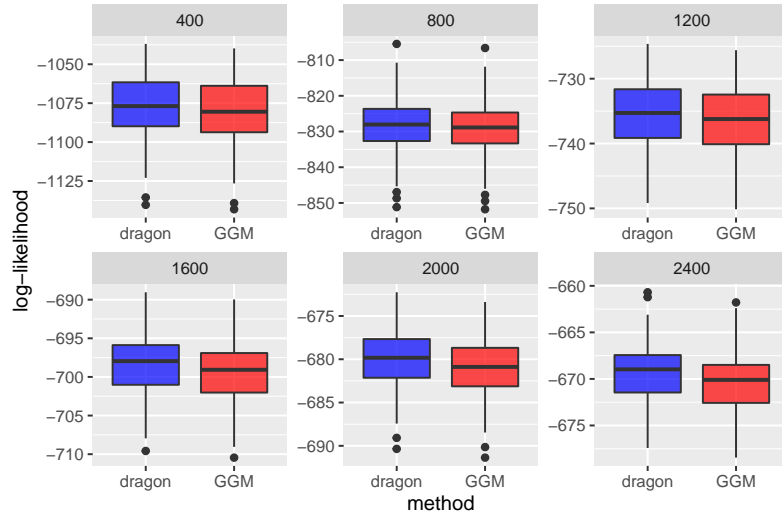


Figure S13: Log-likelihoods of the CBMC dataset for different sample sizes n evaluated on 1000 test samples. The corresponding log-likelihood differences are shown in Figure 5 in the main text.

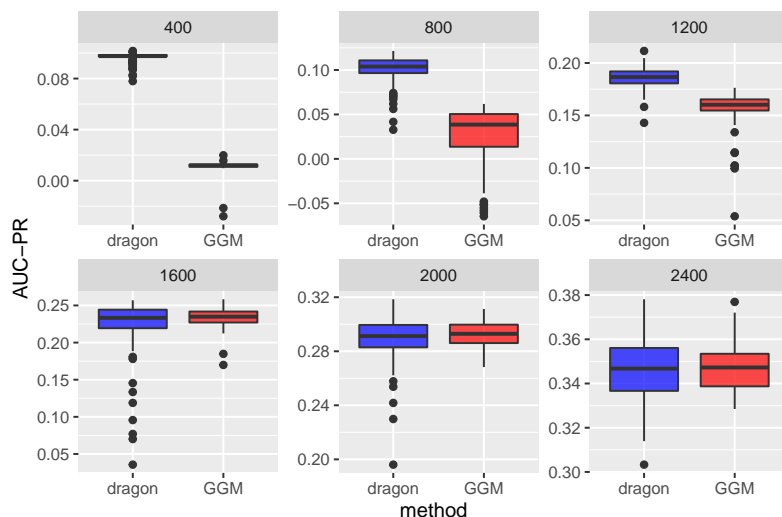


Figure S14: As Figure 3 in the main text but now with average areas under the precision recall curve (AUC-PR) on the y-axis.

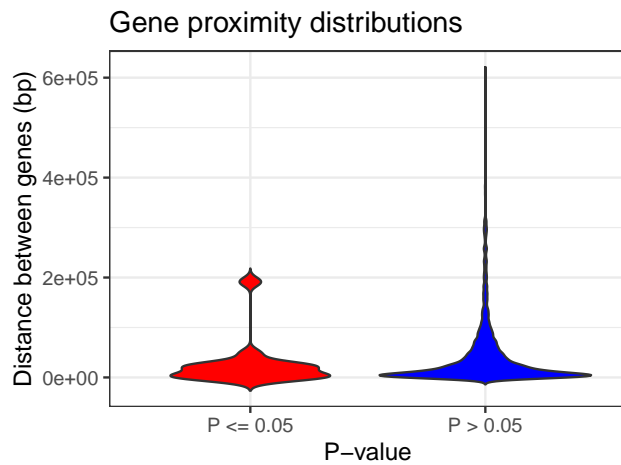


Figure S15: Distribution of significant ($p \leq 0.05$) and non-significant ($p > 0.05$) methylation–methylation edges for which both TFs exist on the same chromosome.

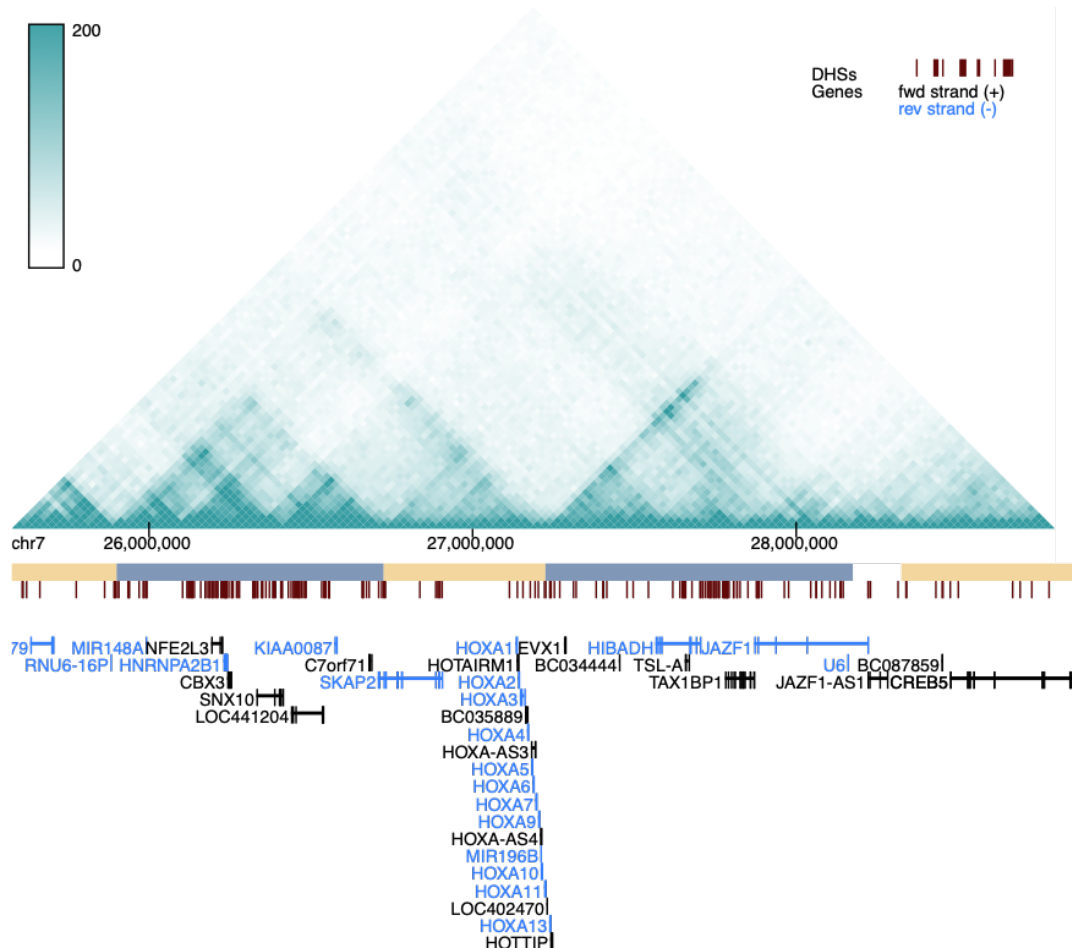


Figure S16: A subnetwork of HOXA genes that are located within the same TAD on chromosome 7 in Hi-C data of the cell line K562, as indicated by the yellow bar. Hi-C data and plots accessed from the 3D Genome Browser [2]. Blue and yellow bars indicate TADs.

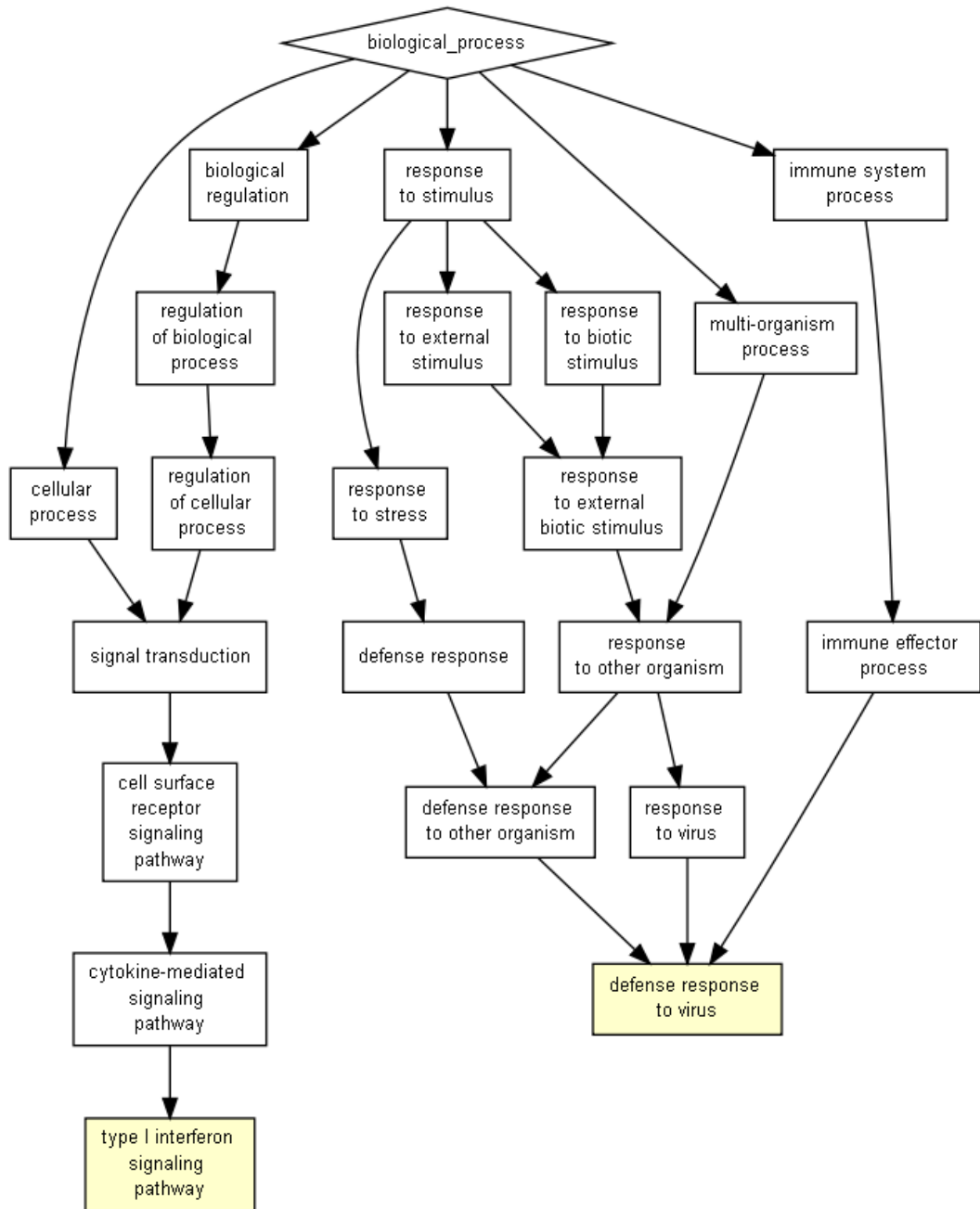


Figure S17: GO enrichment hierarchy for subnetwork 1A. GO enrichment performed using GORILLA [3].

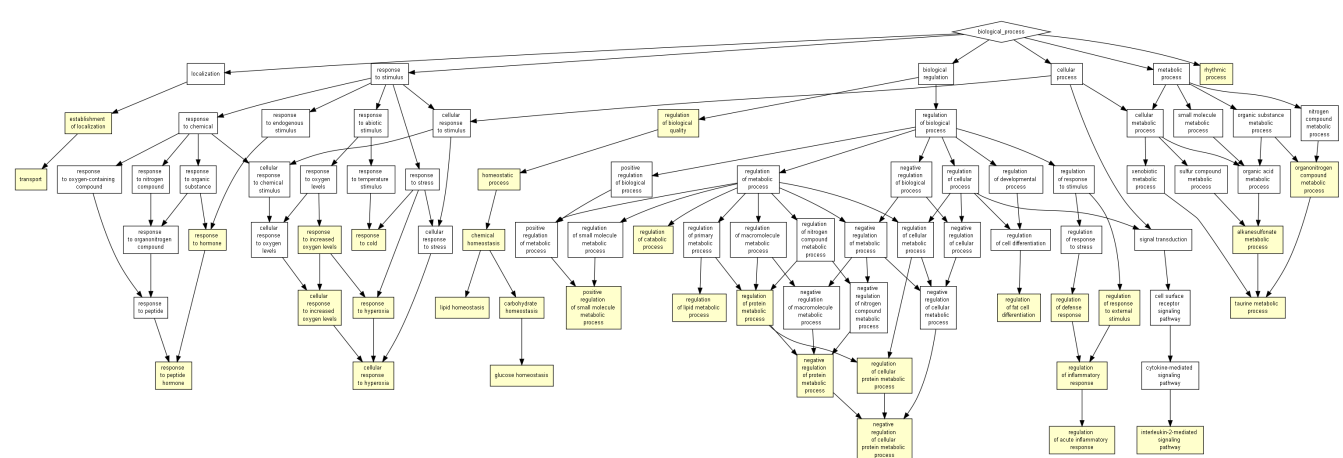


Figure S18: GO enrichment hierarchy for subnetwork 1B.

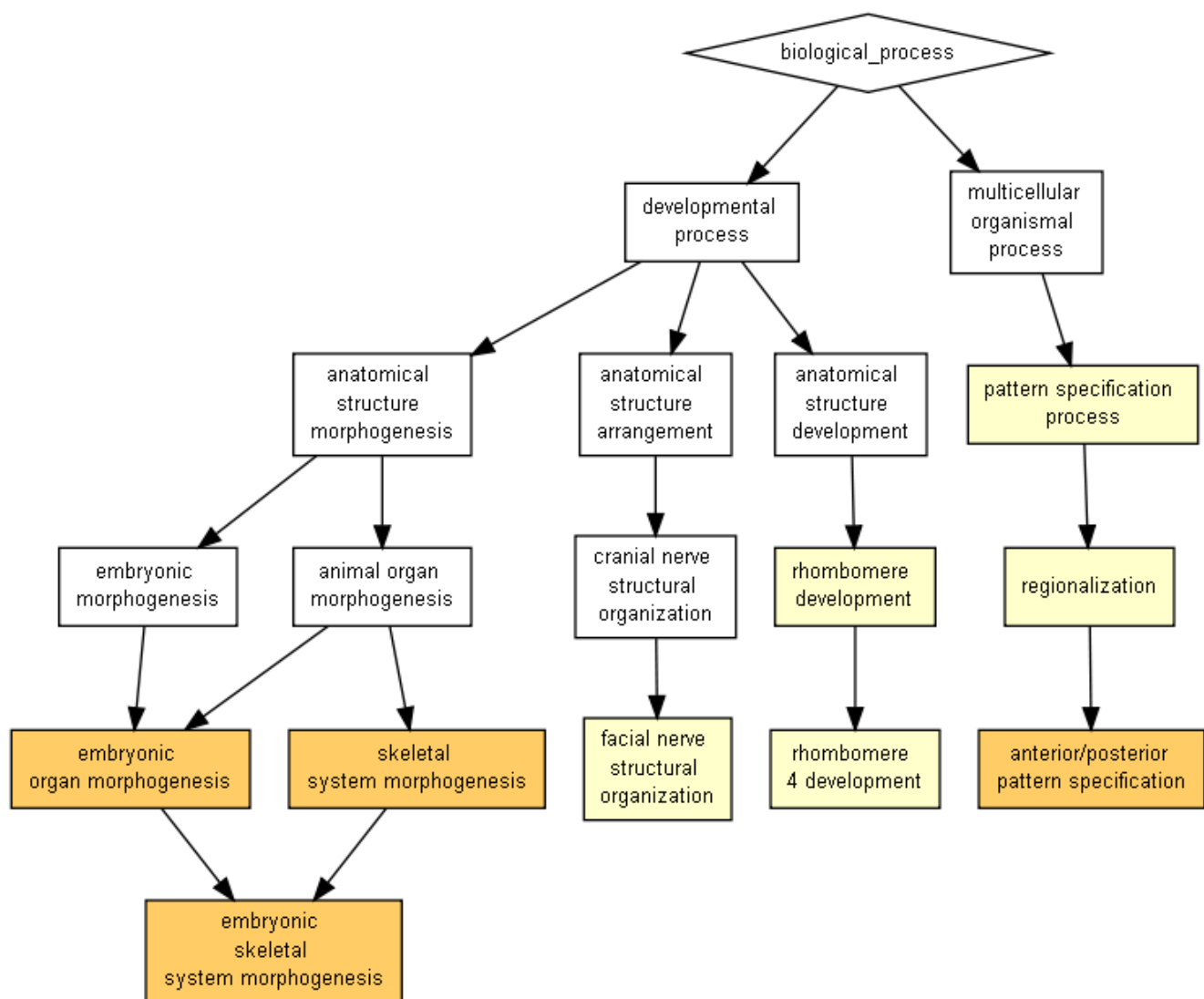


Figure S19: GO enrichment hierarchy for subnetwork 1C.

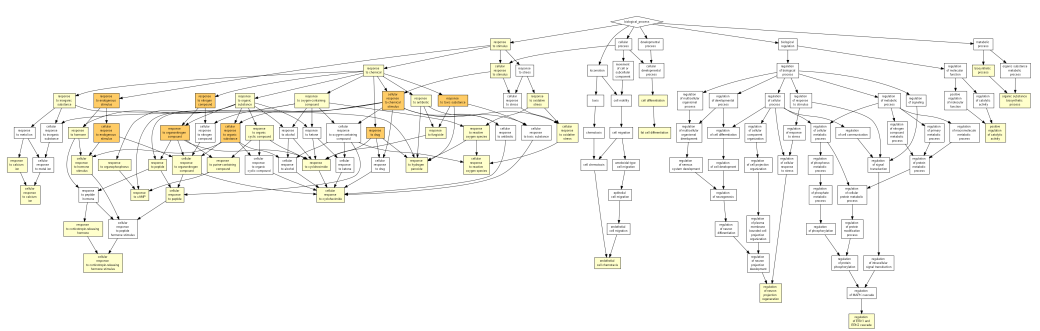


Figure S20: GO enrichment hierarchy for subnetwork 2A.

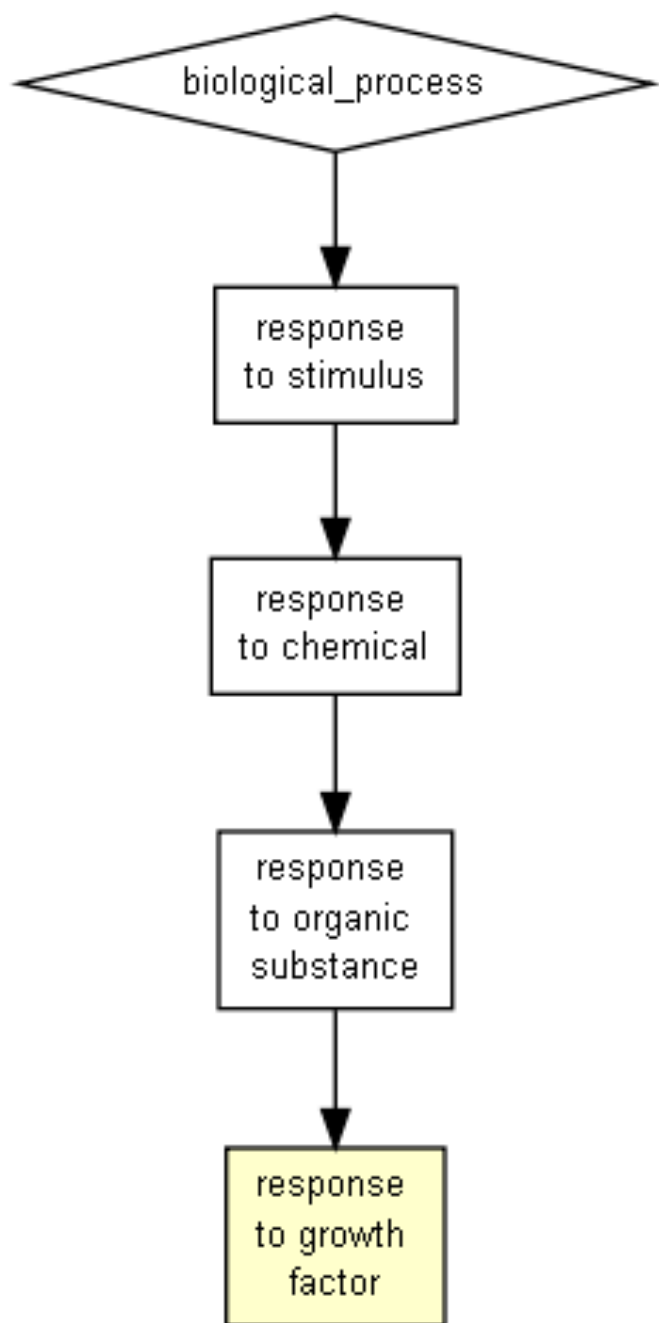


Figure S21: GO enrichment hierarchy for subnetwork 2B.

Table S1: GO enrichment results for subnetwork 1A. N is the total number of genes, B is the total number of genes associated with a specific GO term, n is the number of genes in the target set when appropriate, b is the number of genes in the intersection, and $Enrichment = (b/n) / (B/N)$.

GO Term	Description	P-value	q-value	Enrichment	N	B	n	b	Genes
GO:0051607	defense response to virus	1.72E-4	1E0	11.86	667	9	25	4	[IRF7 - interferon regulatory factor 7, IRF9 - interferon regulatory factor 9, STAT2 - signal transducer and activator of transcription 2, 113kda, STAT1 - signal transducer and activator of transcription 1, 91kda]
GO:0060337	type I interferon signaling pathway	6.24E-4	1E0	8.89	667	12	25	4	[IRF7 - interferon regulatory factor 7, IRF9 - interferon regulatory factor 9, STAT2 - signal transducer and activator of transcription 2, 113kda, STAT1 - signal transducer and activator of transcription 1, 91kda]

Table S2: GO enrichment results for subnetwork 1B. N is the total number of genes, B is the total number of genes associated with a specific GO term, n is the number of genes in the target set when appropriate, b is the number of genes in the intersection, and $Enrichment = (b/n) / (B/N)$.

GO Term	Description	P-value	q-value	Enrichment	N	B	n	b	Genes
GO:0065008	regulation of biological quality	1.22E-5	7.11E-2	3.25	667	154	16	12	[ARNTL - aryl hydrocarbon receptor nuclear translocator-like, KLF15 - kruppel-like factor 15, MLXIPL - mlx interacting protein-like, VTN - vitronectin, CEBPA - ccaat/enhancer binding protein (c/ebp), alpha, STAT5B - signal transducer and activator of transcription 5b, FOXO1 - forkhead box o1, STAT5A - signal transducer and activator of transcription 5a, THRA - thyroid hormone receptor, alpha, RARA - retinoic acid receptor, alpha, PPARG - peroxisome proliferator-activated receptor gamma, NR1D1 - nuclear receptor subfamily 1, group d, member 1]
GO:0048511	rhythmic process	3.9E-5	1.14E-1	6.21	667	47	16	7	[ARNTL - aryl hydrocarbon receptor nuclear translocator-like, TEF - thyrotrophic embryonic factor, HLF - hepatic leukemia factor, STAT5B - signal transducer and activator of transcription 5b, DBP - d site of albumin promoter (albumin d-box) binding protein, PPARG - peroxisome proliferator-activated receptor gamma, NR1D1 - nuclear receptor subfamily 1, group d, member 1]
GO:0009409	response to cold	1.1E-4	2.15E-1	25.01	667	5	16	3	[FOXO1 - forkhead box o1, THRA - thyroid hormone receptor, alpha, PPARG - peroxisome proliferator-activated receptor gamma]
GO:0051246	regulation of protein metabolic process	1.26E-4	1.84E-1	3.75	667	100	16	9	[ARNTL - aryl hydrocarbon receptor nuclear translocator-like, KLF15 - kruppel-like factor 15, MLXIPL - mlx interacting protein-like, VTN - vitronectin, CEBPA - ccaat/enhancer binding protein (c/ebp), alpha, STAT5B - signal transducer and activator of transcription 5b, FOXO1 - forkhead box o1, RARA - retinoic acid receptor, alpha, PPARG - peroxisome proliferator-activated receptor gamma]
GO:0032269	negative regulation of cellular protein metabolic process	1.41E-4	1.65E-1	6.41	667	39	16	6	[KLF15 - kruppel-like factor 15, MLXIPL - mlx interacting protein-like, VTN - vitronectin, CEBPA - ccaat/enhancer binding protein (c/ebp), alpha, FOXO1 - forkhead box o1, RARA - retinoic acid receptor, alpha]

20	GO:0006810	transport	1.44E-4	1.41E-1	5.12	667	57	16	7	[ARNTL - aryl hydrocarbon receptor nuclear translocator-like, CUX1 - cut-like homeobox 1, VTN - vitronectin, STAT5B - signal transducer and activator of transcription 5b, STAT5A - signal transducer and activator of transcription 5a, RARA - retinoic acid receptor, alpha, PPARG - peroxisome proliferator-activated receptor gamma]
	GO:0051248	negative regulation of protein metabolic process	1.64E-4	1.37E-1	6.25	667	40	16	6	[KLF15 - kruppel-like factor 15, MLXIPL - mlx interacting protein-like, VTN - vitronectin, CEBPA - ccaat/enhancer binding protein (c/ebp), alpha, FOXO1 - forkhead box o1, RARA - retinoic acid receptor, alpha, PPARG - peroxisome proliferator-activated receptor gamma]
	GO:0051234	establishment of localization	1.82E-4	1.33E-1	4.95	667	59	16	7	[ARNTL - aryl hydrocarbon receptor nuclear translocator-like, CUX1 - cut-like homeobox 1, VTN - vitronectin, STAT5B - signal transducer and activator of transcription 5b, STAT5A - signal transducer and activator of transcription 5a, RARA - retinoic acid receptor, alpha, PPARG - peroxisome proliferator-activated receptor gamma]
	GO:0045598	regulation of fat cell differentiation	1.97E-4	1.28E-1	8.02	667	26	16	5	[ARNTL - aryl hydrocarbon receptor nuclear translocator-like, CEBPA - ccaat/enhancer binding protein (c/ebp), alpha, FOXO1 - forkhead box o1, PPARG - peroxisome proliferator-activated receptor gamma, NR1D1 - nuclear receptor subfamily 1, group d, member 1]
	GO:0050727	regulation of inflammatory response	1.97E-4	1.15E-1	8.02	667	26	16	5	[VTN - vitronectin, CEBPA - ccaat/enhancer binding protein (c/ebp), alpha, STAT5B - signal transducer and activator of transcription 5b, PPARG - peroxisome proliferator-activated receptor gamma, NR1D1 - nuclear receptor subfamily 1, group d, member 1]
	GO:0033500	carbohydrate homeostasis	2.39E-4	1.27E-1	7.72	667	27	16	5	[KLF15 - kruppel-like factor 15, MLXIPL - mlx interacting protein-like, CEBPA - ccaat/enhancer binding protein (c/ebp), alpha, FOXO1 - forkhead box o1, PPARG - peroxisome proliferator-activated receptor gamma]
	GO:0042593	glucose homeostasis	2.39E-4	1.16E-1	7.72	667	27	16	5	[KLF15 - kruppel-like factor 15, MLXIPL - mlx interacting protein-like, CEBPA - ccaat/enhancer binding protein (c/ebp), alpha, FOXO1 - forkhead box o1, PPARG - peroxisome proliferator-activated receptor gamma]

GO:1901564	organonitrogen compound metabolic process	2.54E-4	1.14E-1	3.97	667	84	16	8	[ARNTL - aryl hydrocarbon receptor nuclear translocator-like, CEBPA - ccaat/enhancer binding protein (c/ebp), alpha, STAT5B - signal transducer and activator of transcription 5b, FOXO1 - forkhead box o1, STAT5A - signal transducer and activator of transcription 5a, PPARG - peroxisome proliferator-activated receptor gamma, RARA - retinoic acid receptor, alpha, NR1D1 - nuclear receptor subfamily 1, group d, member 1]
GO:0032268	regulation of cellular protein metabolic process	4.2E-4	1.75E-1	3.71	667	90	16	8	[ARNTL - aryl hydrocarbon receptor nuclear translocator-like, KLF15 - kruppel-like factor 15, MLXIPL - mlx interacting protein-like, VTN - vitronectin, CEBPA - ccaat/enhancer binding protein (c/ebp), alpha, FOXO1 - forkhead box o1, PPARG - peroxisome proliferator-activated receptor gamma, RARA - retinoic acid receptor, alpha]
GO:0055088	lipid homeostasis	4.38E-4	1.71E-1	9.81	667	17	16	4	[MLXIPL - mlx interacting protein-like, CEBPA - ccaat/enhancer binding protein (c/ebp), alpha, PPARG - peroxisome proliferator-activated receptor gamma, NR1D1 - nuclear receptor subfamily 1, group d, member 1]
GO:0042592	homeostatic process	4.6E-4	1.68E-1	4.29	667	68	16	7	[KLF15 - kruppel-like factor 15, MLXIPL - mlx interacting protein-like, CEBPA - ccaat/enhancer binding protein (c/ebp), alpha, STAT5B - signal transducer and activator of transcription 5b, FOXO1 - forkhead box o1, PPARG - peroxisome proliferator-activated receptor gamma, NR1D1 - nuclear receptor subfamily 1, group d, member 1]
GO:0071455	cellular response to hyperoxia	5.4E-4	1.86E-1	41.69	667	2	16	2	[FOXO1 - forkhead box o1, PPARG - peroxisome proliferator-activated receptor gamma]
GO:0002673	regulation of acute inflammatory response	5.4E-4	1.75E-1	41.69	667	2	16	2	[VTN - vitronectin, PPARG - peroxisome proliferator-activated receptor gamma]
GO:0036295	cellular response to increased oxygen levels	5.4E-4	1.66E-1	41.69	667	2	16	2	[FOXO1 - forkhead box o1, PPARG - peroxisome proliferator-activated receptor gamma]
GO:0036296	response to increased oxygen levels	5.4E-4	1.58E-1	41.69	667	2	16	2	[FOXO1 - forkhead box o1, PPARG - peroxisome proliferator-activated receptor gamma]
GO:0055093	response to hyperoxia	5.4E-4	1.5E-1	41.69	667	2	16	2	[FOXO1 - forkhead box o1, PPARG - peroxisome proliferator-activated receptor gamma]
GO:0019530	taurine metabolic process	5.4E-4	1.43E-1	41.69	667	2	16	2	[STAT5B - signal transducer and activator of transcription 5b, STAT5A - signal transducer and activator of transcription 5a]

22	GO:0038110	interleukin-2-mediated signaling pathway	5.4E-4	1.37E-1	41.69	667	2	16	2	[STAT5B - signal transducer and activator of transcription 5b, STAT5A - signal transducer and activator of transcription 5a]
	GO:0019694	alkanesulfonate metabolic process	5.4E-4	1.31E-1	41.69	667	2	16	2	[STAT5B - signal transducer and activator of transcription 5b, STAT5A - signal transducer and activator of transcription 5a]
	GO:0062013	positive regulation of small molecule metabolic process	5.55E-4	1.3E-1	9.26	667	18	16	4	[MLXIPL - mlx interacting protein-like, FOXO1 - forkhead box o1, PPARG - peroxisome proliferator-activated receptor gamma, NR1D1 - nuclear receptor subfamily 1, group d, member 1]
	GO:0043434	response to peptide hormone	6.44E-4	1.45E-1	6.32	667	33	16	5	[KLF15 - kruppel-like factor 15, FOXO1 - forkhead box o1, STAT5B - signal transducer and activator of transcription 5b, STAT5A - signal transducer and activator of transcription 5a, PPARG - peroxisome proliferator-activated receptor gamma]
	GO:0048878	chemical homeostasis	6.61E-4	1.43E-1	4.90	667	51	16	6	[KLF15 - kruppel-like factor 15, MLXIPL - mlx interacting protein-like, CEBPA - ccaat/enhancer binding protein (c/ebp), alpha, FOXO1 - forkhead box o1, PPARG - peroxisome proliferator-activated receptor gamma, NR1D1 - nuclear receptor subfamily 1, group d, member 1]
	GO:0009725	response to hormone	7.9E-4	1.65E-1	3.94	667	74	16	7	[KLF15 - kruppel-like factor 15, STAT5B - signal transducer and activator of transcription 5b, FOXO1 - forkhead box o1, STAT5A - signal transducer and activator of transcription 5a, PPARG - peroxisome proliferator-activated receptor gamma, RARA - retinoic acid receptor, alpha, NR1D1 - nuclear receptor subfamily 1, group d, member 1]
	GO:0009894	regulation of catabolic process	8.57E-4	1.72E-1	5.96	667	35	16	5	[ARNTL - aryl hydrocarbon receptor nuclear translocator-like, MLXIPL - mlx interacting protein-like, CEBPA - ccaat/enhancer binding protein (c/ebp), alpha, FOXO1 - forkhead box o1, THRA - thyroid hormone receptor, alpha]
	GO:0032101	regulation of response to external stimulus	9.81E-4	1.91E-1	5.79	667	36	16	5	[VTN - vitronectin, CEBPA - ccaat/enhancer binding protein (c/ebp), alpha, STAT5B - signal transducer and activator of transcription 5b, PPARG - peroxisome proliferator-activated receptor gamma, NR1D1 - nuclear receptor subfamily 1, group d, member 1]

GO:0019216	regulation of lipid metabolic process	9.81E-4	1.85E-1	5.79	667	36	16	5	[MLXIPL - mlx interacting protein-like, STAT5B - signal transducer and activator of transcription 5b, THRA - thyroid hormone receptor, alpha, PPARG - peroxisome proliferator-activated receptor gamma, NR1D1 - nuclear receptor subfamily 1, group d, member 1]
GO:0031347	regulation of defense response	9.81E-4	1.79E-1	5.79	667	36	16	5	[VTN - vitronectin, CEBPA - ccaat/enhancer binding protein (c/ebp), alpha, STAT5B - signal transducer and activator of transcription 5b, PPARG - peroxisome proliferator-activated receptor gamma, NR1D1 - nuclear receptor subfamily 1, group d, member 1]

Table S3: GO enrichment results for subnetwork 1C. N is the total number of genes, B is the total number of genes associated with a specific GO term, n is the number of genes in the target set when appropriate, b is the number of genes in the intersection, and $Enrichment = (b/n) / (B/N)$.

GO Term	Description	P-value	q-value	Enrichment	N	B	n	b	Genes
GO:0048704	embryonic skeletal system morphogenesis	3.9E-7	2.28E-3	11.12	667	35	12	7	[HOXB3 - homeobox b3, HOXB2 - homeobox b2, HOXB1 - homeobox b1, HOXB8 - homeobox b8, HOXB7 - homeobox b7, HOXB6 - homeobox b6, HOXB5 - homeobox b5]
GO:0048705	skeletal system morphogenesis	8.68E-7	2.54E-3	9.98	667	39	12	7	[HOXB3 - homeobox b3, HOXB2 - homeobox b2, HOXB1 - homeobox b1, HOXB8 - homeobox b8, HOXB7 - homeobox b7, HOXB6 - homeobox b6, HOXB5 - homeobox b5]
GO:0048562	embryonic organ morphogenesis	3.9E-6	7.6E-3	8.11	667	48	12	7	[HOXB3 - homeobox b3, HOXB2 - homeobox b2, HOXB1 - homeobox b1, HOXB8 - homeobox b8, HOXB7 - homeobox b7, HOXB6 - homeobox b6, HOXB5 - homeobox b5]
GO:0009952	anterior/posterior pattern specification	5.52E-6	8.05E-3	6.01	667	74	12	8	[HOXB3 - homeobox b3, HOXB2 - homeobox b2, RBPJ - recombination signal binding protein for immunoglobulin kappa j region, HOXB1 - homeobox b1, HOXB8 - homeobox b8, HOXB7 - homeobox b7, HOXB6 - homeobox b6, HOXB5 - homeobox b5]
GO:0021546	rhombomere development	8.67E-5	1.01E-1	27.79	667	6	12	3	[HOXB3 - homeobox b3, HOXB2 - homeobox b2, HOXB1 - homeobox b1]
GO:0003002	regionalization	9.77E-5	9.51E-2	4.16	667	107	12	8	[HOXB3 - homeobox b3, HOXB2 - homeobox b2, HOXB1 - homeobox b1, RBPJ - recombination signal binding protein for immunoglobulin kappa j region, HOXB8 - homeobox b8, HOXB7 - homeobox b7, HOXB6 - homeobox b6, HOXB5 - homeobox b5]
GO:0007389	pattern specification process	2.97E-4	2.47E-1	3.59	667	124	12	8	[HOXB3 - homeobox b3, HOXB2 - homeobox b2, HOXB1 - homeobox b1, RBPJ - recombination signal binding protein for immunoglobulin kappa j region, HOXB8 - homeobox b8, HOXB7 - homeobox b7, HOXB6 - homeobox b6, HOXB5 - homeobox b5]
GO:0021570	rhombomere 4 development	2.97E-4	2.17E-1	55.58	667	2	12	2	[HOXB2 - homeobox b2, HOXB1 - homeobox b1]
GO:0021612	facial nerve structural organization	8.83E-4	5.73E-1	37.06	667	3	12	2	[HOXB2 - homeobox b2, HOXB1 - homeobox b1]

Table S4: GO enrichment results for subnetwork 2A. N is the total number of genes, B is the total number of genes associated with a specific GO term, n is the number of genes in the target set when appropriate, b is the number of genes in the intersection, and $Enrichment = (b/n) / (B/N)$.

GO Term	Description	P-value	q-value	Enrichment	N	B	n	b	Genes
GO:0010243	response to organonitrogen compound	4.52E-7	2.64E-3	5.46	667	64	21	11	[EGR1 - early growth response 1, FOSB - fbj murine osteosarcoma viral oncogene homolog b, FOS - fbj murine osteosarcoma viral oncogene homolog, NR4A2 - nuclear receptor subfamily 4, group a, member 2, NR4A3 - nuclear receptor subfamily 4, group a, member 3, JUN - jun proto-oncogene, EGR2 - early growth response 2, NR4A1 - nuclear receptor subfamily 4, group a, member 1, JUNB - jun b proto-oncogene, KLF2 - kruppel-like factor 2 (lung), KLF4 - kruppel-like factor 4 (gut)]
GO:1901698	response to nitrogen compound	5.36E-7	1.56E-3	5.38	667	65	21	11	[EGR1 - early growth response 1, FOSB - fbj murine osteosarcoma viral oncogene homolog b, FOS - fbj murine osteosarcoma viral oncogene homolog, NR4A2 - nuclear receptor subfamily 4, group a, member 2, NR4A3 - nuclear receptor subfamily 4, group a, member 3, JUN - jun proto-oncogene, EGR2 - early growth response 2, NR4A1 - nuclear receptor subfamily 4, group a, member 1, JUNB - jun b proto-oncogene, KLF2 - kruppel-like factor 2 (lung), KLF4 - kruppel-like factor 4 (gut)]
GO:0071310	cellular response to organic substance	7.36E-7	1.43E-3	3.36	667	142	21	15	[EGR2 - early growth response 2, JUN - jun proto-oncogene, EGR3 - early growth response 3, JUNB - jun b proto-oncogene, KLF2 - kruppel-like factor 2 (lung), RUNX2 - runt-related transcription factor 2, SOX17 - sry (sex determining region y)-box 17, KLF4 - kruppel-like factor 4 (gut), EGR1 - early growth response 1, FOSB - fbj murine osteosarcoma viral oncogene homolog b, FOS - fbj murine osteosarcoma viral oncogene homolog, NR4A2 - nuclear receptor subfamily 4, group a, member 2, NR4A3 - nuclear receptor subfamily 4, group a, member 3, NR5A2 - nuclear receptor subfamily 5, group a, member 2, NR4A1 - nuclear receptor subfamily 4, group a, member 1]

GO:0071495	cellular response to endogenous stimulus	7.5E-7	1.1E-3	4.59	667	83	21	12	[EGR1 - early growth response 1, FOSB - fbj murine osteosarcoma viral oncogene homolog b, FOS - fbj murine osteosarcoma viral oncogene homolog, NR4A2 - nuclear receptor subfamily 4, group a, member 2, NR4A3 - nuclear receptor subfamily 4, group a, member 3, JUN - jun proto-oncogene, EGR3 - early growth response 3, NR4A1 - nuclear receptor subfamily 4, group a, member 1, JUNB - jun b proto-oncogene, RUNX2 - runt-related transcription factor 2, KLF2 - kruppel-like factor 2 (lung), KLF4 - kruppel-like factor 4 (gut)]
GO:0042493	response to drug	2.27E-6	2.66E-3	5.38	667	59	21	10	[EGR1 - early growth response 1, FOSB - fbj murine osteosarcoma viral oncogene homolog b, FOS - fbj murine osteosarcoma viral oncogene homolog, NR4A2 - nuclear receptor subfamily 4, group a, member 2, NR4A3 - nuclear receptor subfamily 4, group a, member 3, JUN - jun proto-oncogene, JUNB - jun b proto-oncogene, EMX2 - empty spiracles homeobox 2, KLF2 - kruppel-like factor 2 (lung), KLF4 - kruppel-like factor 4 (gut)]
GO:0070887	cellular response to chemical stimulus	2.33E-6	2.26E-3	3.09	667	154	21	15	[EGR2 - early growth response 2, JUN - jun proto-oncogene, EGR3 - early growth response 3, JUNB - jun b proto-oncogene, KLF2 - kruppel-like factor 2 (lung), RUNX2 - runt-related transcription factor 2, SOX17 - sry (sex determining region y)-box 17, KLF4 - kruppel-like factor 4 (gut), EGR1 - early growth response 1, FOSB - fbj murine osteosarcoma viral oncogene homolog b, FOS - fbj murine osteosarcoma viral oncogene homolog, NR4A2 - nuclear receptor subfamily 4, group a, member 2, NR4A3 - nuclear receptor subfamily 4, group a, member 3, NR5A2 - nuclear receptor subfamily 5, group a, member 2, NR4A1 - nuclear receptor subfamily 4, group a, member 1]

GO:0009719	response to endogenous stimulus	3.45E-6	2.88E-3	3.62	667	114	21	13	[EGR2 - early growth response 2, JUN - jun proto-oncogene, EGR3 - early growth response 3, JUNB - jun b proto-oncogene, KLF2 - kruppel-like factor 2 (lung), RUNX2 - runt-related transcription factor 2, KLF4 - kruppel-like factor 4 (gut), EGR1 - early growth response 1, FOSB - fbj murine osteosarcoma viral oncogene homolog b, FOS - fbj murine osteosarcoma viral oncogene homolog, NR4A2 - nuclear receptor subfamily 4, group a, member 2, NR4A3 - nuclear receptor subfamily 4, group a, member 3, NR4A1 - nuclear receptor subfamily 4, group a, member 1]
GO:0009636	response to toxic substance	8.19E-6	5.98E-3	7.94	667	28	21	7	[EGR1 - early growth response 1, FOS - fbj murine osteosarcoma viral oncogene homolog, NR4A2 - nuclear receptor subfamily 4, group a, member 2, NR4A3 - nuclear receptor subfamily 4, group a, member 3, JUN - jun proto-oncogene, KLF2 - kruppel-like factor 2 (lung), KLF4 - kruppel-like factor 4 (gut)]
GO:0042221	response to chemical	1.39E-5	8.99E-3	2.52	667	202	21	16	[EGR2 - early growth response 2, JUN - jun proto-oncogene, EGR3 - early growth response 3, JUNB - jun b proto-oncogene, KLF2 - kruppel-like factor 2 (lung), RUNX2 - runt-related transcription factor 2, SOX17 - sry (sex determining region y)-box 17, KLF4 - kruppel-like factor 4 (gut), EGR1 - early growth response 1, FOSB - fbj murine osteosarcoma viral oncogene homolog b, FOS - fbj murine osteosarcoma viral oncogene homolog, NR4A2 - nuclear receptor subfamily 4, group a, member 2, NR4A3 - nuclear receptor subfamily 4, group a, member 3, NR5A2 - nuclear receptor subfamily 5, group a, member 2, EMX2 - empty spiracles homeobox 2, NR4A1 - nuclear receptor subfamily 4, group a, member 1]
GO:0006979	response to oxidative stress	1.83E-5	1.07E-2	9.07	667	21	21	6	[FOS - fbj murine osteosarcoma viral oncogene homolog, NR4A2 - nuclear receptor subfamily 4, group a, member 2, NR4A3 - nuclear receptor subfamily 4, group a, member 3, JUN - jun proto-oncogene, KLF2 - kruppel-like factor 2 (lung), KLF4 - kruppel-like factor 4 (gut)]

GO:0051716	cellular response to stimulus	2.28E-5	1.21E-2	2.43	667	209	21	16	[EGR2 - early growth response 2, JUN - jun proto-oncogene, EGR3 - early growth response 3, JUNB - jun b proto-oncogene, KLF2 - kruppel-like factor 2 (lung), RUNX2 - runt-related transcription factor 2, KLF4 - kruppel-like factor 4 (gut), SOX17 - sry (sex determining region y)-box 17, EGR1 - early growth response 1, FOSB - fbj murine osteosarcoma viral oncogene homolog b, FOS - fbj murine osteosarcoma viral oncogene homolog, NR4A2 - nuclear receptor subfamily 4, group a, member 2, NR4A3 - nuclear receptor subfamily 4, group a, member 3, NR5A2 - nuclear receptor subfamily 5, group a, member 2, NR4A1 - nuclear receptor subfamily 4, group a, member 1, ATF3 - activating transcription factor 3]
GO:0043435	response to corticotropin-releasing hormone	2.7E-5	1.31E-2	31.76	667	3	21	3	[NR4A2 - nuclear receptor subfamily 4, group a, member 2, NR4A3 - nuclear receptor subfamily 4, group a, member 3, NR4A1 - nuclear receptor subfamily 4, group a, member 1]
GO:0071376	cellular response to corticotropin-releasing hormone stimulus	2.7E-5	1.21E-2	31.76	667	3	21	3	[NR4A2 - nuclear receptor subfamily 4, group a, member 2, NR4A3 - nuclear receptor subfamily 4, group a, member 3, NR4A1 - nuclear receptor subfamily 4, group a, member 1]
GO:0010035	response to inorganic substance	3.32E-5	1.38E-2	6.54	667	34	21	7	[FOSB - fbj murine osteosarcoma viral oncogene homolog b, FOS - fbj murine osteosarcoma viral oncogene homolog, NR4A3 - nuclear receptor subfamily 4, group a, member 3, JUN - jun proto-oncogene, JUNB - jun b proto-oncogene, KLF2 - kruppel-like factor 2 (lung), KLF4 - kruppel-like factor 4 (gut)]

GO:0010033	response to organic substance	3.63E-5	1.41E-2	2.53	667	188	21	15	[EGR2 - early growth response 2, JUN - jun proto-oncogene, EGR3 - early growth response 3, JUNB - jun b proto-oncogene, KLF2 - kruppel-like factor 2 (lung), RUNX2 - runt-related transcription factor 2, SOX17 - sry (sex determining region y)-box 17, KLF4 - kruppel-like factor 4 (gut), EGR1 - early growth response 1, FOSB - fbj murine osteosarcoma viral oncogene homolog b, FOS - fbj murine osteosarcoma viral oncogene homolog, NR4A2 - nuclear receptor subfamily 4, group a, member 2, NR4A3 - nuclear receptor subfamily 4, group a, member 3, NR5A2 - nuclear receptor subfamily 5, group a, member 2, NR4A1 - nuclear receptor subfamily 4, group a, member 1]
GO:0000302	response to reactive oxygen species	4.6E-5	1.68E-2	10.59	667	15	21	5	[FOS - fbj murine osteosarcoma viral oncogene homolog, NR4A3 - nuclear receptor subfamily 4, group a, member 3, JUN - jun proto-oncogene, KLF2 - kruppel-like factor 2 (lung), KLF4 - kruppel-like factor 4 (gut)]
GO:0071277	cellular response to calcium ion	4.72E-5	1.62E-2	15.88	667	8	21	4	[FOSB - fbj murine osteosarcoma viral oncogene homolog b, FOS - fbj murine osteosarcoma viral oncogene homolog, JUN - jun proto-oncogene, JUNB - jun b proto-oncogene]
GO:0051592	response to calcium ion	4.72E-5	1.53E-2	15.88	667	8	21	4	[FOSB - fbj murine osteosarcoma viral oncogene homolog b, FOS - fbj murine osteosarcoma viral oncogene homolog, JUN - jun proto-oncogene, JUNB - jun b proto-oncogene]
GO:0034599	cellular response to oxidative stress	6.55E-5	2.01E-2	9.93	667	16	21	5	[FOS - fbj murine osteosarcoma viral oncogene homolog, NR4A2 - nuclear receptor subfamily 4, group a, member 2, JUN - jun proto-oncogene, KLF2 - kruppel-like factor 2 (lung), KLF4 - kruppel-like factor 4 (gut)]

30	GO:0050896	response to stimulus	9.26E-5	2.7E-2	1.93	667	296	21	18	[EGR2 - early growth response 2, JUN - jun proto-oncogene, EGR3 - early growth response 3, JUNB - jun b proto-oncogene, KLF2 - kruppel-like factor 2 (lung), RUNX2 - runt-related transcription factor 2, SOX17 - sry (sex determining region y)-box 17, KLF4 - kruppel-like factor 4 (gut), EGR1 - early growth response 1, FOSB - fbj murine osteosarcoma viral oncogene homolog b, FOS - fbj murine osteosarcoma viral oncogene homolog, NR4A2 - nuclear receptor subfamily 4, group a, member 2, NR4A3 - nuclear receptor subfamily 4, group a, member 3, NR5A2 - nuclear receptor subfamily 5, group a, member 2, EMX2 - empty spiracles homeobox 2, NR4A1 - nuclear receptor subfamily 4, group a, member 1, ATF3 - activating transcription factor 3, BATF3 - basic leucine zipper transcription factor, atf-like 3]
	GO:1901652	response to peptide	1.43E-4	3.96E-2	5.29	667	42	21	7	[EGR1 - early growth response 1, NR4A2 - nuclear receptor subfamily 4, group a, member 2, NR4A3 - nuclear receptor subfamily 4, group a, member 3, EGR2 - early growth response 2, NR4A1 - nuclear receptor subfamily 4, group a, member 1, KLF2 - kruppel-like factor 2 (lung), KLF4 - kruppel-like factor 4 (gut)]
	GO:0009725	response to hormone	1.56E-4	4.13E-2	3.86	667	74	21	9	[EGR1 - early growth response 1, FOSB - fbj murine osteosarcoma viral oncogene homolog b, FOS - fbj murine osteosarcoma viral oncogene homolog, NR4A2 - nuclear receptor subfamily 4, group a, member 2, NR4A3 - nuclear receptor subfamily 4, group a, member 3, JUN - jun proto-oncogene, EGR2 - early growth response 2, NR4A1 - nuclear receptor subfamily 4, group a, member 1, JUNB - jun b proto-oncogene]
	GO:0051591	response to cAMP	2.09E-4	5.31E-2	11.55	667	11	21	4	[FOSB - fbj murine osteosarcoma viral oncogene homolog b, FOS - fbj murine osteosarcoma viral oncogene homolog, JUN - jun proto-oncogene, JUNB - jun b proto-oncogene]
	GO:0046683	response to organophosphorus	2.09E-4	5.09E-2	11.55	667	11	21	4	[FOSB - fbj murine osteosarcoma viral oncogene homolog b, FOS - fbj murine osteosarcoma viral oncogene homolog, JUN - jun proto-oncogene, JUNB - jun b proto-oncogene]

GO:0032870	cellular response to hormone stimulus	2.26E-4	5.28E-2	4.94	667	45	21	7	[FOSB - fbj murine osteosarcoma viral oncogene homolog b, FOS - fbj murine osteosarcoma viral oncogene homolog, NR4A2 - nuclear receptor subfamily 4, group a, member 2, NR4A3 - nuclear receptor subfamily 4, group a, member 3, JUN - jun proto-oncogene, NR4A1 - nuclear receptor subfamily 4, group a, member 1, JUNB - jun b proto-oncogene]
GO:0034614	cellular response to reactive oxygen species	3.07E-4	6.9E-2	10.59	667	12	21	4	[FOS - fbj murine osteosarcoma viral oncogene homolog, JUN - jun proto-oncogene, KLF2 - kruppel-like factor 2 (lung), KLF4 - kruppel-like factor 4 (gut)]
GO:0014074	response to purine-containing compound	3.07E-4	6.64E-2	10.59	667	12	21	4	[FOSB - fbj murine osteosarcoma viral oncogene homolog b, FOS - fbj murine osteosarcoma viral oncogene homolog, JUN - jun proto-oncogene, JUNB - jun b proto-oncogene]
GO:1901700	response to oxygen-containing compound	3.99E-4	8.33E-2	2.82	667	124	21	11	[EGR1 - early growth response 1, FOSB - fbj murine osteosarcoma viral oncogene homolog b, FOS - fbj murine osteosarcoma viral oncogene homolog, NR4A2 - nuclear receptor subfamily 4, group a, member 2, NR4A3 - nuclear receptor subfamily 4, group a, member 3, JUN - jun proto-oncogene, EGR2 - early growth response 2, NR4A1 - nuclear receptor subfamily 4, group a, member 1, JUNB - jun b proto-oncogene, KLF2 - kruppel-like factor 2 (lung), KLF4 - kruppel-like factor 4 (gut)]
GO:0045444	fat cell differentiation	4.37E-4	8.8E-2	6.90	667	23	21	5	[NR4A2 - nuclear receptor subfamily 4, group a, member 2, NR4A3 - nuclear receptor subfamily 4, group a, member 3, EGR2 - early growth response 2, NR4A1 - nuclear receptor subfamily 4, group a, member 1, KLF4 - kruppel-like factor 4 (gut)]
GO:0046677	response to antibiotic	4.37E-4	8.51E-2	6.90	667	23	21	5	[EGR1 - early growth response 1, NR4A3 - nuclear receptor subfamily 4, group a, member 3, JUN - jun proto-oncogene, KLF2 - kruppel-like factor 2 (lung), KLF4 - kruppel-like factor 4 (gut)]
GO:0070372	regulation of ERK1 and ERK2 cascade	5.08E-4	9.57E-2	15.88	667	6	21	3	[JUN - jun proto-oncogene, ATF3 - activating transcription factor 3, KLF4 - kruppel-like factor 4 (gut)]

32	GO:1901576	organic substance biosynthetic process	5.15E-4	9.4E-2	2.20	667	202	21	14	[EGR2 - early growth response 2, JUN - jun proto-oncogene, RUNX2 - runt-related transcription factor 2, KLF4 - kruppel-like factor 4 (gut), SOX17 - sry (sex determining region y)-box 17, EGR1 - early growth response 1, FOSB - fbj murine osteosarcoma viral oncogene homolog b, FOS - fbj murine osteosarcoma viral oncogene homolog, NR4A2 - nuclear receptor subfamily 4, group a, member 2, NR4A3 - nuclear receptor subfamily 4, group a, member 3, NR5A2 - nuclear receptor subfamily 5, group a, member 2, NR4A1 - nuclear receptor subfamily 4, group a, member 1, ATF3 - activating transcription factor 3, BATF3 - basic leucine zipper transcription factor, atf-like 3]
	GO:0009058	biosynthetic process	5.15E-4	9.12E-2	2.20	667	202	21	14	[EGR2 - early growth response 2, JUN - jun proto-oncogene, RUNX2 - runt-related transcription factor 2, KLF4 - kruppel-like factor 4 (gut), SOX17 - sry (sex determining region y)-box 17, EGR1 - early growth response 1, FOSB - fbj murine osteosarcoma viral oncogene homolog b, FOS - fbj murine osteosarcoma viral oncogene homolog, NR4A2 - nuclear receptor subfamily 4, group a, member 2, NR4A3 - nuclear receptor subfamily 4, group a, member 3, NR5A2 - nuclear receptor subfamily 5, group a, member 2, NR4A1 - nuclear receptor subfamily 4, group a, member 1, ATF3 - activating transcription factor 3, BATF3 - basic leucine zipper transcription factor, atf-like 3]
	GO:0043085	positive regulation of catalytic activity	5.41E-4	9.29E-2	6.62	667	24	21	5	[EGR1 - early growth response 1, NR4A2 - nuclear receptor subfamily 4, group a, member 2, JUN - jun proto-oncogene, SOX7 - sry (sex determining region y)-box 7, KLF4 - kruppel-like factor 4 (gut)]
	GO:0042542	response to hydrogen peroxide	5.96E-4	9.94E-2	9.07	667	14	21	4	[NR4A3 - nuclear receptor subfamily 4, group a, member 3, JUN - jun proto-oncogene, KLF2 - kruppel-like factor 2 (lung), KLF4 - kruppel-like factor 4 (gut)]

GO:0014070	response to organic cyclic compound	8.08E-4	1.31E-1	3.53	667	72	21	8	[EGR1 - early growth response 1, FOSB - fbj murine osteosarcoma viral oncogene homolog b, FOS - fbj murine osteosarcoma viral oncogene homolog, NR4A3 - nuclear receptor subfamily 4, group a, member 3, JUN - jun proto-oncogene, JUNB - jun b proto-oncogene, KLF2 - kruppel-like factor 2 (lung), KLF4 - kruppel-like factor 4 (gut)]
GO:0030154	cell differentiation	8.55E-4	1.35E-1	1.68	667	340	21	18	[EGR2 - early growth response 2, JUN - jun proto-oncogene, JUNB - jun b proto-oncogene, KLF2 - kruppel-like factor 2 (lung), RUNX2 - runt-related transcription factor 2, SOX17 - sry (sex determining region y)-box 17, KLF4 - kruppel-like factor 4 (gut), EGR1 - early growth response 1, FOS - fbj murine osteosarcoma viral oncogene homolog, NR4A2 - nuclear receptor subfamily 4, group a, member 2, CREM - camp responsive element modulator, NR4A3 - nuclear receptor subfamily 4, group a, member 3, NR5A2 - nuclear receptor subfamily 5, group a, member 2, SOX7 - sry (sex determining region y)-box 7, EMX2 - empty spiracles homeobox 2, NR4A1 - nuclear receptor subfamily 4, group a, member 1, ATF3 - activating transcription factor 3, BATF3 - basic leucine zipper transcription factor, atf-like 3]
GO:0071417	cellular response to organonitrogen compound	8.84E-4	1.36E-1	4.76	667	40	21	6	[EGR1 - early growth response 1, NR4A2 - nuclear receptor subfamily 4, group a, member 2, NR4A3 - nuclear receptor subfamily 4, group a, member 3, NR4A1 - nuclear receptor subfamily 4, group a, member 1, KLF2 - kruppel-like factor 2 (lung), KLF4 - kruppel-like factor 4 (gut)]
GO:0071409	cellular response to cycloheximide	9.45E-4	1.42E-1	31.76	667	2	21	2	[KLF2 - kruppel-like factor 2 (lung), KLF4 - kruppel-like factor 4 (gut)]
GO:0070570	regulation of neuron projection regeneration	9.45E-4	1.38E-1	31.76	667	2	21	2	[PRRX1 - paired related homeobox 1, KLF4 - kruppel-like factor 4 (gut)]
GO:0060992	response to fungicide	9.45E-4	1.35E-1	31.76	667	2	21	2	[KLF2 - kruppel-like factor 2 (lung), KLF4 - kruppel-like factor 4 (gut)]
GO:0046898	response to cycloheximide	9.45E-4	1.31E-1	31.76	667	2	21	2	[KLF2 - kruppel-like factor 2 (lung), KLF4 - kruppel-like factor 4 (gut)]
GO:0035767	endothelial cell chemotaxis	9.45E-4	1.28E-1	31.76	667	2	21	2	[EGR3 - early growth response 3, NR4A1 - nuclear receptor subfamily 4, group a, member 1]

GO:1901653 cellular response to peptide 9.66E-4 1.28E-1 5.88 667 27 21 5 [NR4A2 - nuclear receptor subfamily 4, group a, member 2, NR4A3 - nuclear receptor subfamily 4, group a, member 3, NR4A1 - nuclear receptor subfamily 4, group a, member 1, KLF2 - kruppel-like factor 2 (lung), KLF4 - kruppel-like factor 4 (gut)]

Table S5: GO enrichment results for subnetwork 2B. N is the total number of genes, B is the total number of genes associated with a specific GO term, n is the number of genes in the target set when appropriate, b is the number of genes in the intersection, and $Enrichment = (b/n) / (B/N)$.

GO Term	Description	P-value	q-value	Enrichment	N	B	n	b	Genes
GO:0070848	response to growth factor	6.39E-4	1E0	5.02	667	42	19	6	[ID1 - inhibitor of dna binding 1, dominant negative helix-loop-helix protein, GATA6 - gata binding protein 6, CDC5L - cell division cycle 5-like, ELK1 - elk1, member of ets oncogene family, SOX6 - sry (sex determining region y)-box 6, DLX5 - distal-less homeobox 5]

References

- [1] Marlon Stoeckius, Christoph Hafemeister, William Stephenson, Brian Houck-Loomis, Pratip K Chattopadhyay, Harold Swerdlow, Rahul Satija, and Peter Smibert. Simultaneous epitope and transcriptome measurement in single cells. *Nature methods*, 14(9):865, 2017.
- [2] Yanli Wang, Fan Song, Bo Zhang, Lijun Zhang, Jie Xu, Da Kuang, Daofeng Li, Mayank NK Choudhary, Yun Li, Ming Hu, et al. The 3d genome browser: a web-based browser for visualizing 3d genome organization and long-range chromatin interactions. *Genome biology*, 19(1):1–12, 2018.
- [3] Eran Eden, Roy Navon, Israel Steinfeld, Doron Lipson, and Zohar Yakhini. Gorilla: a tool for discovery and visualization of enriched go terms in ranked gene lists. *BMC bioinformatics*, 10(1):48, 2009.